*Astronomy & Astrophysics* manuscript no. paper1-9
April 18, 2011


# Deep UBVRI observations of a field within ELAIS-S1

## – the Stockholm VIMOS Supernova Survey III.

L. Mencía Trinchant[1], J. Melinder[1], T. Dahlén[2], G. Östlin[1], C. Fransson[1], S. Nasoudi-Shoar[3], M. Hayes[4], and S. Mattila[1,5]

[1] Stockholm Observatory, AlbaNova University Center, 106 91 Stockholm, Sweden
e-mail: laia@astro.su.se
[2] Space Telescope Science Institute, 3700 San Martin Drive, Baltimore, MD 21218
[3] Argelander-Institut für Astronomie, Universität Bonn, Auf dem Hügel 71, 53121 Bonn, Germany
[4] Observatory of Geneva, University of Geneva, 51 chemin des Maillettes, 1290 Versoix, Switzerland
[5] Tuorla Observatory, Dpt. of Physics and Astronomy, University of Turku, Väisälantie 20, FI-21500 Piikkiö, Finland

**ABSTRACT**

*Context.* The Stockholm VIMOS Supernova Survey (SVISS) is an optical broad-band photometry survey, aimed at the search for distant (redshifts z≃0.7) supernovae, which are detected by means of monthly imaging in $R$ and $I$ bands with the VIMOS instrument on the ESO VLT. The distances of the supernovae are estimated using photometric redshifts facilitated by additional $U, B$ and $V$ imaging also with VIMOS. In this paper we present the deep stacked imaging data in all these bands and a catalogue of galaxies extending to very faint magnitudes.
*Aims.* We discuss the various steps followed to create a galaxy catalog, including the reduction and stacking of the data, astrometric and photometric calibration and source detections. We derived completeness, corrected number counts and color selected Lyman break galaxies. Raw number counts are also calculated. Finally, making use of a template fitting code, photometric redshifts are derived.
*Methods.* UBVRI deep imaging of a 4x56 arcmin$^2$ field within the ELAIS-S1 field is presented in this paper. The data reduction has been done with a dedicated MIDAS pipeline. The final images have been weighted by their seeing, which was found to optimise depth and spatial resolution. Source detection and phortometry was done using SExtractor. The photometric accuracy was tested by comparing the colors of the sources to stellar libraries and redshifted galaxy templates. A mixture of synthetic point-like and extended sources are simulated in order to estimate completeness. Derived number counts have been compared to the results of similar surveys. Lyman break galaxy candidates were selected using color criteria: UBR, BRI, BVI and VRI, and their numbers computed and compared to other surveys. We have obtained photometric redshifts by spectral energy distribution template fitting. The photometric redshifts were calibrated using a sample of galaxies in the HDF-S with available spectroscopic redshifts that have also been observed with the same filter set as used here.
*Results.* Using a seeing weighted method to combine the science frames resulted in an increase of the number of faint objects detected and minimizing the photometric errors. The astrometric accuracy is ≃0.4″ with respect to 2MASS and 5$\sigma$ limiting magnitudes for UBVRI are ≃28.2, 29.3, 28.3, 28.5 and 27.2 respectively (Vega). The computed galaxy number counts are in good agreement with previous works, with the U band counts of this survey being one of the deepest ever obtained. The raw number counts from broadband color selected Lyman break galaxies show a good agreement for the U and B dropouts with other surveys. Photometric redshifts have a scatter of $\sigma_z$=0.085 with a 9.1% fraction of outliers.
*Conclusions.* We derive deep number counts which are found to be consistent with previous works, reproducing the bright and faint ends. Especially, the stacked deep U and I band data are found to present a comptetetive combination of depth and area, comparable to HDF observations. As well as V band, comparable to Subaru and the Lockman hole observations. Our U and B dropouts are within the expected redshift range, with mean values of 3 and 3.8 respectively.

**Key words.** surveys - catalogues - techniques: image processing - galaxies: photometry

## 1. Introduction

To understand formation and evolution processes of individual galaxies, formation of galaxy clusters, cosmic large-scale structures are some of the goals in extragalactic astronomy. To study galaxy formation and evolution, statistically significant samples of both bright and faint objects are needed. This, in turn, requires deep imaging and spectroscopy over wide areas of the sky. In pursuit of this data, many galaxy surveys have been conducted. These include e.g. COSMOS (Taniguchi et al. 2007), CFHTLS (Nuijten et al. 2005), SDSS (Stoughton et al. 2002), MUSYC (Gawiser et al. 2006), VIRMOS (Le Fèvre et al. 2004), GOODS (Giavalisco et al. 2004).

The analysis of number counts is a tool that can be used to test the geometry of space, the evolution of the galaxy population and the evolution of structure in the universe (Tinsley (1972), Brown & Tinsley (1974)). The number-magnitude relation is a function of the luminosity-distance and therefore can provide information on the cosmological model, taking into account the influence of the luminosity functions, spectra and evolution of all types of galaxies. They also provide a quick check on data quality because they are sensitive to photometric calibration errors, detection completeness and spurious detections. Computed number counts in specific bands can be found in e.g. Metcalfe

*Send offprint requests to*: L. Mencía Trinchant

et al. (2001), Radovich et al. (2004), Furusawa et al. (2008) and Jeon et al. (2010).

Lyman-break galaxies are star-forming galaxies at high redshift that are selected by using colors that probe the position of the Lyman limit and Ly$\alpha$ absorption blueward of 1216Å in restframe. A color selection scheme can be used to select galaxies at certain redshift ranges, a technique described by Partridge & Peebles (1967) and first used successfully by Steidel & Hamilton (1993). At high redshifts, z$\gtrsim$2.5, the 912Å Lyman-continuum discontinuity shifts into the optical window, the U band at 3600Å, and is detectable with broad-band photometry. Radiation at shorter wavelengths than this break is almost completely absorbed by neutral gas surrounding star-forming regions while the spectrum remains bright at longer wavelengths. By placing filters on each side of the break, one shortward of the 912Å break, the second between this break and the Ly$\alpha$ forest, and the third one redwards of it, high-redshift objects can be identified by their red colors. As this break shifts through the different bands, different redshift ranges can be selected. For example, similar criteria for B-band dropouts can be defined, which would produce galaxy candidates at redshifts $3.5 \lesssim z \lesssim 4.5$. Studies on them have been done by Steidel et al. (1996), Giavalisco (2002), Yoshida et al. (2006), Yoshida et al. (2008) and Rafelski et al. (2009) among others.

However, the red colors of the selected objects can also be due to other reasons, e.g. they can be low redshift objects with a high amount of dust extinction or red foreground stars. The LBG technique is thus sensitive to contamination of stars and galaxies at completely different distances than the population being studied and care has to be taken to reject possible interlopers.

Due to technological and telescope time constraints, obtaining spectroscopic redshifts for more than a limited and relatively bright fraction of galaxies will remain impractical for the foreseeable future. The alternative technique is to use photometric redshifts. The photometric redshift technique allows the calculation of redshifts of a large number of faint sources in a relatively short amount of time. This idea was first used by Baum (1962), who originally applied it to measure redshifts for elliptical galaxies in distant clusters.

Two broad categories of photometric redshifts estimators are widely in use: template-fitting, first suggested by Loh & Spillar (1986), and training set methods, first implemented by Connolly et al. (1995). The first method relies mainly on shifting spectral energy distribution (SED) templates, either theoretical or empirical, selected from one of the many library of templates available, to a given redshift until finding the template that best matches the observed fluxes. It bases its efficiency on the fit of the overall shape of spectra and on the detection of strong spectral features. Codes based on this method are Hyperz by Bolzonella et al. (2000), ZEBRA by Feldmann et al. (2006), BPZ by Benítez (2000) and the probability friends-of-friends algorithm by Li & Yee (2008). The second method requires objects with known spectroscopic redshift to derive an empirical relation between them and photometric observables. In general a large number of sources is needed to cover every galaxy type at all redshifts. Empirical training methods include artificial neural networks like Collister & Lahav (2004), Abdalla et al. (2008) and Zhang et al. (2009), linear and non-linear polynomial fitting by Hsieh et al. (2005) and support vector machines by Wadadekar (2005).

Both methods have drawbacks. The training methods need a large set of spectroscopic redshifts to define a realistic unbiased relation between spectroscopic and photometric observables, which requires investing large amounts of telescope time and are not able to reach faint objects. In the case of template-fitting methods one of the drawbacks is the use of templates, usually produced for low redshift galaxies and used to measure high redshift sources, hence assuming that low and high-redshifts galaxies have similar properties.

Together with redshift values, most existing photometric codes also provide estimates on age, star fomation history, mass and star formation rates, to name some of the possible output values.

Other studies can be performed with this kind of optical survey, like clustering and luminosity function measurements.

Galaxy groups and clusters can be observationally identified trough different techniques, e.g. by their X-ray emission, the collection of galaxies close by, strong features in the gravitational shear field. One of these techniques is the angular two-point correlation function, which is based on counting pairs of galaxies at given angular separation and normalize the results with the number of pairs expected from a random distribution (e.g. Pović et al. 2009). Another way of finding clusters or groups of galaxies is through colors. These congregations of galaxies tend to host early-types, which have small dispersion in color and form a characteristic red sequence containing the brightest, reddest galaxies at a given redshift. Clustering measurements have been performed by, e.g., Hansen et al. (2005), Kashikawa et al. (2006), van Breukelen et al. (2006) and Wilson (2003).

The luminosity function measures the number of galaxies per unit volume as a function of luminosity, which is closely related to star formation processes, and therefore can be used to probe galaxy formation and evolution (e.g. Bell et al. 2003; Oesch et al. 2010; van der Burg et al. 2010). Luminosity function measurements have been determined by Gabasch et al. (2004), Dahlen et al. (2005), Faber et al. (2007) and Christlein et al. (2009) among others

Joining these already existing surveys, we present the Stockholm VIMOS Supernova Survey (SVISS). The aim of the survey is to discover and classify supernovae (SNe) at redshifts higher than z≃0.5 (Melinder et al. 2008, 2011 (submitted)), through variations on their magnitudes. Since this is an imaging survey, the SNe study is based only on photometry and the information that can be derived from it, e.g. photometric redshifts, peak magnitudes, shape of light curves. A follow-up program to obtain spectroscopic redshifts for the SN host galaxies is underway. The SNe will be used to determine rates of different SN types to z≃1 as a function of redshift (Melinder et al., in prep.). The properties of host galaxies and dependence with their environment, will be presented in Mencía Trinchant et al. (in prep.).

In this paper we describe observations, reduction, calibration and analysis of the U, B, V, R and I observations of the ELAIS-S1field. Estimates of the completeness, number counts and selection of Lyman Break galaxies are presented together with photometric redshifts. Section 2 briefly describes the observational planning and different filters used. In section 3 the data reduction and final products of the survey, such as stacking of the data, are presented, and it also describes calibration, alignment and astrometry. Section 4 deals with source detection, photometry and the creation of the catalogues. Section 5 contains the completeness estimates and number counts, which are compared to other authors' values. Section 6 deals with Lyman break galaxy selections through color combinations, number counts of dropouts compared to available published data and their redshift distribution. In section 7 we discuss the determination of photometric redshifts and the calibration of the method. Finally, in section 8 a brief summary of the paper is presented.

All magnitudes from here onwards are in the Vega system.

## 2. Data set

The observations of the field, located within the ELAIS-S1 field La Franca et al. (2004) at $\alpha$(J2000)=00:32:12.9 and $\delta$(J=2000)=-44:36:27, were carried out with the VLT telescope in Paranal, Chile, of 8.2 meters diameter, with the VIMOS instrument (Le Fèvre et al. 2003) in imaging mode, allowing deep imaging in a relative short period of time and with good quality over a large field of view.

The field of view is divided into four quadrants, named b1, a2, a3 and b4, due to the CCD configuration, see Figure 1. Each quadrant is 7x8 square arcminutes with a separation between them of approximately 2′.

Five broad band filters were used for the observations, U, B, V, R and I. The transmission curves of the five filters are given in Figure 2 [1].

This project is a large ESO program with 114 hours of observations (ESO programme ID:167.D-0492, with Claes Fransson as P.I.), spanning over a period of four years, from 2003 to 2006. The project also includes Chandra Deep Field-south Giacconi et al. (2001) observations with VIMOS R and I filters, which will be approached in future papers. Table 1 shows the total time invested for each band and the exposure time of a single image.

The survey was designed for monitoring the observed field in R and I bands. This strategy is optimum for detecting SNe at redshift z≃0.5-1 since they emit mostly in the rest-frame optical (B and V) bands. The SN magnitudes need to have changed enough to allow detection. With a spacing of around 30 days between runs the average fading of a SN at z=0.8 is ≃0.5 to 1 magnitude. This way, a source detected in three consecutive epochs in these bands should have faded ≃1 magnitude.

The R and I observations are divided in epochs. There is a total of nine epochs, with seven of them conducted between July and December 2004 in monthly intervals. These are the supernova search epochs. One epoch obtained a year earlier, acts as a reference epoch for the SN search, while a final one, taken a half year after the last search epoch, serves as a control epoch to eliminate non-transient variable sources, such as AGN. More detailed information is facilitated in Table 1. This table also contains the minimum and maximum seeing for each monthly observations. If the maximum seeing is higher that 1.2″, the image in question will not be used, so we have not written any value on the table above that limit.

The observations in the U, B and V bands are distributed differently than the R and I bands (see Table 1), since they are not used for detection nor for typing of SNe. These bands will be used to gather information on the host galaxies of the SNe and measure their photometric redshift.

Since the VIMOS CCDs has strong fringing in the I band, we optimised the observations so that the fringe pattern could be efficiently and cleanly removed from the science images. Each I band epoch was designed to contain 4 one hour OBs each consisting of 6 exposures of 480s, hence in total 24 exposures taken under a duration of 4 hours. These 24 exposures were arranged in a grid of 6x4 positions (x and y) with size 18″×30″. Hence the point spacing is on average 6″. However, in order to minimise the influence of correlated residuals the grid was adjusted so that none of the vectors connecting any two points in the grid had the same length and angle to within 1″, and the gridpoints were stepped through in a way to get both long and short offsets between subsequent exposures. Furthermore, the grid was subject to small adjustments from epoch to epoch to futher optimise the performance when constructing deep I band images by stacking all the individual epochs. In the R band, the same strategy was used although the number of exposures per epoch was only half of the in the I band.

Since the average grid spacing is 6″, this means that objects a few times larger than this will partially overlap when stacking the images in order to make the fringe map. Although large sources are (by survey construction) rare, signs of imperfect fringe subtraction may be seen in some places. A larger grid spacing would have meant a smaller FOV covered to a uniform depth and would have caused problems in finding guide stars that could be used for entire OBs.

Along with science frames, standard, flat fields and bias frames were taken during the observations.

## 3. Reduction process

The raw images obtained are processed using an in-house pipeline written in the MIDAS programming environment, and optimised for the SVISS project. The basic redcution steps are described below:

Bias: The first step of the reduction process is the creation of a masterbias, made by averaging the bias frames obtained for a given day or epoch.

Masks: Parts of the area of the CCD are subject to vignetting, e.g. by the guide probe in which case it may change from frame to frame. In addition, there are bad pixels which need to be

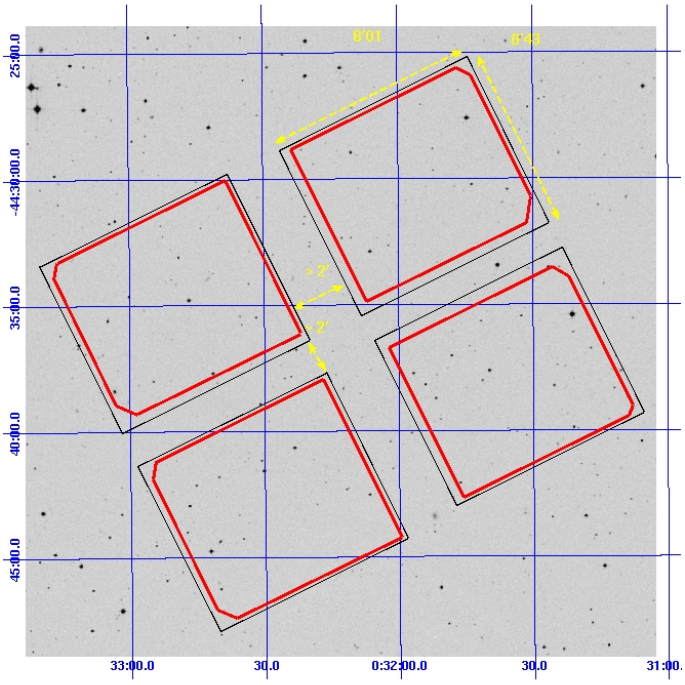


**Fig. 1.** Field of view. Black thin lines represent the CCD and its four sections, while red thick lines correspond to the real size and shape of the images. The flat edges show the vignetting effect present in the observations.

[1] For more information see: http://eso.org/sci/facilities/paranal/

**Table 1.** Dates of observations for U, B, V, R and I. Includes total and individual exposure times, and lowest and highest seeing value for the monthly observations.

| Band | Date of observation | Seeing [″] | Exposure time [s] | Total time [h] |
|---|---|---|---|---|
| U | 2003 Nov 23, 24 | 0.8-1.2 | | |
| | 2004 Jul 23; Oct 12 | 0.55-0.79; 0.55-0.66 | | |
| | 2005 Sep 5, 8; Oct 8, Nov 4, 29; Dec 19, 28 | 0.58-0.89; 0.95-1.17; 0-86-1.2; 0.67-1.2 | | |
| | 2006 Aug 18, 19 | 0.6-1.2 | 1020 | 16 |
| B | 2003 Nov 26 | 0.68-1.2 | | |
| | 2004 Oct 11; Nov 15 | 0.54-0.93; 0.59-0.80 | | |
| | 2005 Jul 10, 11; Sep 6, 12; Oct 7; Nov 1, 4, 28 | 0.74-1.2; 0.55-1.2; 0.63-0.9; 0.52-1.2 | | |
| | 2006 Jul 4; Aug 19 | 0.79-1; 0.52-0.87 | 1020 | 13 |
| V | 2003 Nov 27; Dec 20 | 0.53-1.2; 0.8-0.96 | | |
| | 2005 Oct 21; Nov 1 | 0.77-1.01; 0.73-1.14 | 750 | 7 |
| R | 2003 Jul 6, 7, 21, 26, 28 | 0.63-0.89 | | |
| | 2004 Jun 23, 25; Jul 15, 18, 20; Aug 14, 15; Sep 19, 20 | 0.5-0.75; 0.45-0.94; 0.47-1.2; 0.74-1.2 | | |
| | 2004 Oct 7 ,9, 10, 11; Nov 6; Dec 5, 6 | 0.61-1.2; 0.56-0.98; 0.68-0.97 | | |
| | 2005 Aug 7 | 0.49-0.61 | 480 | 19 |
| I | 2003 Jul 6, 7 ,21, 26, 28 | 0.50-1.2 | | |
| | 2004 Jun 22, 23, 24; Jul 15, 16 20; Aug 13, 14, 15; Sep 18, 19, 20 | 0.46-0.8; 0.44-1.2; 0.46-1.2; 0.57-0.94 | | |
| | 2004 Oct 5, 8, 9, 10, 11; Nov 5, 6, 12, 13; Dec 5, 6, 7, 10 | 0.57-1.2; 0.49-0.9; 0.53-1.2 | | |
| | 2005 Aug 29; Sep 5, 10 | 0.70-0.91; 0.51-1.00 | 480 | 41 |

Note: any image with seeing higher than 1.2 ″ has been rejected, hence we do not include seeing values larger than that in this table.

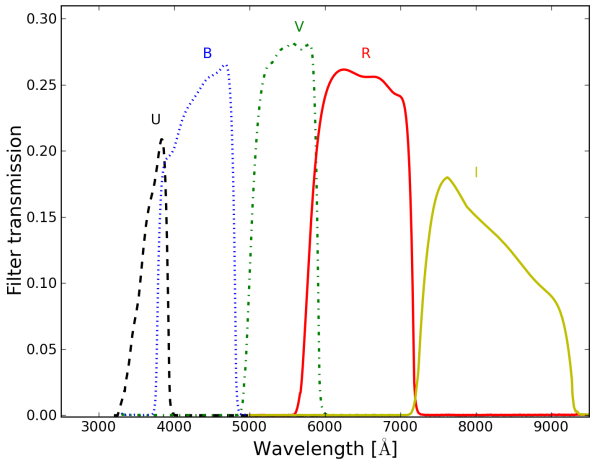


**Fig. 2.** Transmission curves for UBVR and I bands for the b1 quadrant.

masked out. For each frame, a mask was made in which regions with a signal lower than 85% of that of the sky mode were flagged. A cosmic ray filter was run on each frame and all identified cosmic rays were also flagged in the mask for each frame.

Flat fielding: For each band and epoch, a standard twilight sky flat field was created. For the R band we also create a 'superflat' which was made in the following way: the bias subtracted and flat fielded science frames were normalised to the same sky level and combined with a clipped median. While this combined image gives a good representation of the CCD illumination for the science images, it is rather noisy and has residuals near positions of bright stars. We therefore divided this superflat with the normal twilight flat, and fitted a second order polynomial to it, which was then multiplied with the twilight flat to produce a combined flat. This procedure was followed in the R band. In the U, B, and V filters, the normal twilight flat produced good results - moreover, these frames were always obtained with the moon below the horizon and have very low sky count levels. In the I band, we followed a special procedure due to the strong fringing pattern of the VIMOS CCDs at near infra-red red wavelengths.

De-fringing: Due to the presence of strong fringe patterns in the I band images, which are not purely multiplicative and hence not removed by the flat field division, a fringe map was created by taking a clipped median of all I band science frames for a given night. We then defringe the I band frames by subtracting the fringe map scaled to the sky mode of the science frames. One fringe map per night is typically made, in the cases with a significant difference between airmass in the images and if we have enough frames, multiple fringe maps were made for the same night.

Co-addition of science frames: Each science frame is first debiased. Then vignetted areas, bad pixels and cosmic ray affected pixels are masked. The images are then divided by the appropriate flat field and, only for the I band, defringed. Next, the images are corrected for airmass and atmospheric extinction (using the extinction coefficients supplied by ESO for FORS) and normalised to 1s exposure time. The images are then aligned and combined. The combined image is the (weigthed) union of the ingredient frames, meaning that the image is shallower towards the edges where the effective exposure times is smaller due to the dithering.

Our combining procedure allows for different kinds of weightings, e.g. for optimisation of depth vs seeing. Other surveys have also weighted their frames before combining them to improve the final results, e.g. Heidt et al. (2003) used a seeing derived weight, Gabasch et al. (2008) used a S/N combination as a weighting factor, while Furusawa et al. (2008) flux-weighted average values in each pixel with a 3 $\sigma$ clipping process and Kashikawa et al. (2004) stacked their frames with weights according to their relative throughput. In our pipeline, images can be weighted by:

– inverse of the noise computed on the reduced images
– inverse of the noise computed on the raw images
– inverse of the average seeing of the reference sources
– inverse of the signal-to-noise ratio
– weight of one for all images

We tested which method produced the best results by comparing the number of sources and deepth of the images. A comparison between these different methods is seen in Figure 3. The best weighting method is obviously the inverse of the seeing, allowing us to gain depth, diminishing the errors of the faintest magnitudes by 12.5% and increasing the number of sources by 10%. It is also the method which, for a given set of images, produce that sharpest final image.

The alignment involves shifting the images and a small possible rotation and change of plate scale due to the changing airmass, and is also applied to the masks. The masks are in turn added to produce a combined mask as well as a weighted combined mask, in which each mask is weighted in the same way as its corresponding image. The weighted mask can then be multiplied with the exposure time per frame to yield an exposure map.

We did not use all the available science frames to create the final stacked images: first all images with full width at high maximum (hereafter FWHM) FWHM > 1.2″ were rejected. We divided the science frames in two groups, one which contained all images with a seeing FWHM< 0.9″ and the other contained all images with FWHM< 1.2″. The different sets were then combined into two images per passband, one "sharp" and one "deep". The final choice between these was made based on the similarity of the seeings between the different passbands, since this implies a minimum of convolution needed in order to make the aperture and resolution matched catalogues used for derivation of photometric reshifts. The third column of Table 2 shows the total exposure time for each band and quadrant used for the creation of the deep images and the image FWHM is given in column four. Figure 4 is a RGB color composite image of the a2 quadrant.

### 3.1. Photometric calibration

Most of the data was obtained during nights which were declared as photometric. For the photometric nights we reduced the standard star frames provided as part of the standard calibration plan for service mode observations with our pipeline and performed aperture photometry with the IRAF task PHOT. These instrumental magnitudes were then compared to their catalogued values in the Vega system to Stetson[2] (Stetson 2000) when possible, otherwise to Landolt[3] (Landolt 1992). In this way we determined the zero points for observations obtained during particular night.

We define a set of approximately 50 suitably bright and usaturated sources that are used as secondary standards to calibrate the deep stacked images and data observed in non photometric conditions (or for nights when standard stars were not obtained). Here we use an aperture of 2 times the FWHM, and aperture corrections for obtaining total magnitudes (or more correctly at radii 10 times the FWHM) of -0.109 for U band, -0.114 for B, -0.082 for V, -0.113 for R and -0.101 for I.

[2] See http://www3.cadc-ccda.hia-iha.nrc-cnrc.gc.ca/community/STETSON/standards/

[3] See http://www.cfht.hawaii.edu/ObsInfo/Standards/Landolt/

### 3.2. Astrometric calibration

Since the reduction pipeline alters the world coordinate system (WCS) of the images, we first use the KARMA [4] (Gooch 1996) software to internally correct the WCS of the final images and make sure it is consitstent between the different passbands. Finally, we use the software GAIA[5] to calibrate our WCS against the the 2MASS catalogue. The number of sources in the 2MASS catalogue that fall in field is around twelve per quadrant, but most of them are saturated except for the U band. Therefore we make the absolute calibration in the U-band. From the RMS we estimate that absolute position accuracy is 0.356″.In Figure 5 we show the difference in R.A. and DEC between world coordinates of sources in both 2MASS and our images.

## 4. Object detection and photometry

We used SourceExtractor (hereafter SE), (Bertin & Arnouts 1996), to detect objects in the images. Two different catalogues are obtained, one to derive photometric redshifts from and the other a full galaxy catalogue to study the photometric properties of the detections. The detections are done in a different way for the two catalogues.

For the photometric redshift catalog, a combined I+R image is created by summing the two frames. This image is used as a detection image for the dual mode runs, containing only the sources present in I or R images. On the other hand, for the galaxy catalog, SE is run independently for each deep image, in single mode (except when detecting in convolved images). In this case the final catalogue has every existing source in any of the images. When we run SE in convolved images we use the dual mode, using the I+R or normal deep images as detection

[4] http://www.atnf.csiro.au/computing/software/karma/

[5] http://astro.dur.ac.uk/≃pdraper/gaia/gaia.html

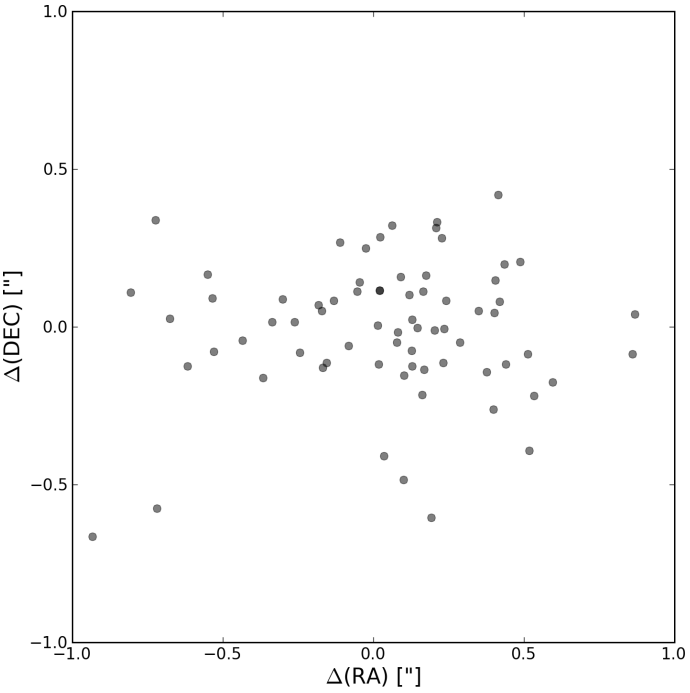


**Fig. 5.** Astrometric accuracy of the observed VIMOS field for the U band. Δ(RA) and Δ(DEC) are calibration residuals between the observed objects and 2MASS sources in the direction of right ascension and declination, respectively.

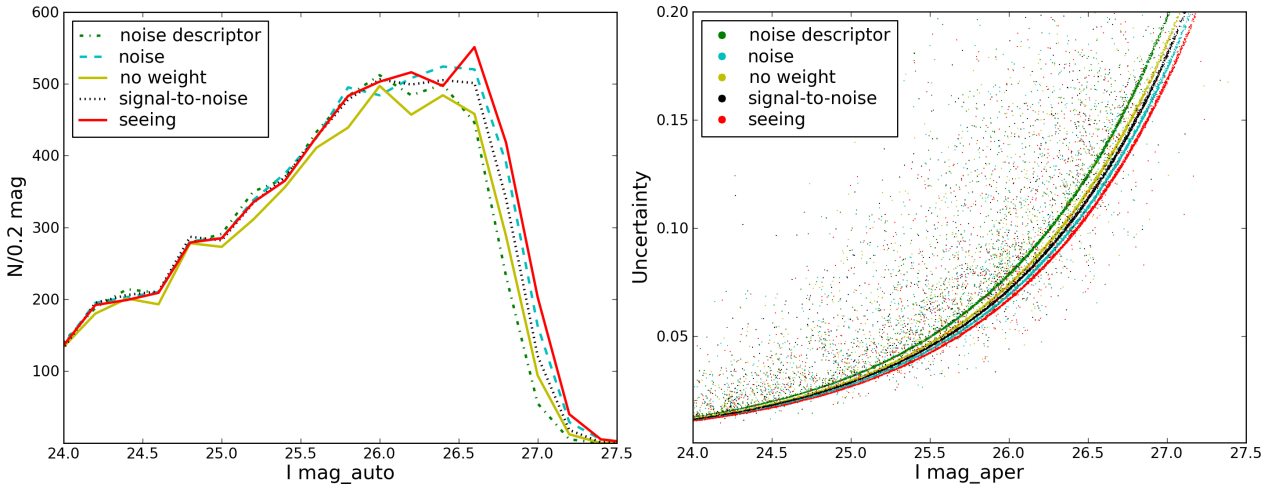


**Fig. 3.** Left panel: number counts comparing the different weighting methods using 0.2 magnitude bins. Right panel: comparison between the different weighting methods magnitudes and their errors. From left to right the different weighting methods are the inverse of the noise computed on the reduced images, no weight, inverse of the signal-to-noise, inverse of the noise computed on the raw images and finally the inverse of the seeing.

frames. These convolved frames are created using the `Pyraf` task `PSFMATCH`, where we have used ≃50 star-like objects to compute the convolution kernels.

A list of the parameters used for detections is given in Table 10, which can be found in the Appendix. The parameters in bold are values that change from image to image. The detection threshold and analysis threshold are such that the number of spurious detections is lower than 5%.These values are calculated by dividing the number of detections of the inverted image by those of the real image, and when we reach the imposed condition we set the parameters to these values. We set the SE aperture radius to be $2 \times FWHM$ and the minimum area required for a source to be detected to be $FWHM^2 \times \frac{\pi}{4}$.

Deep UBVRI catalogue: The deep UBVRI catalogue is created in two different steps. First we run SE in single mode for each deep image using their values of seeing, gain, aperture, threshold and others, as shown in Table 10. The second step consists of running it in dual mode, using the deep images for object detection, and their agnate convolved images for photometry measurements. In this case, each input parameter is set to its corresponding value, the detection parameters are given by the original deep images' values, while the photometry parameters are described by the convolved images, hence all of them have a common aperture.

The output parameters of this first step are listed in Table 11. This catalogue is used to determine limiting magnitudes, quality testing the photometry, and completeness and number counts studies.

Deep I+R catalogue: To increase the signal-to-noise ratio of the sources, especially of the faintest sources, a combined I+R image is created by summing the two frames. We also co-added the I and R masks, to create a combined mask. We run the code in dual mode using this image as a detection image and the deep images as photometry images. The same is then repeated for the convolved frames. The input parameters are given in Table 10, the ones defined by the detection image correspond to the combined I+R, while the photometry parameters are given by the deep or the convolved images.

The output parameters are the same as for the galaxy catalog. This catalogue is used to compute photometric redshifts and do dropout selections.

Coordinate matching: Once we have the different SE ouputs for the different bands, we match them using their pixel coordinates. We allow a distance between sources in the different bands of three pixels in radius. Then the two final catalogues are produced. The deep UBVRI catalogue contains ∼50000 and the deep I+R catalogue ∼35000.

To deal with the effects of source blending in crowded fields, we inspected the images and corrected the photometric data of the sources affected by it redoing the detection without using any gaussian smoothing (setting the SE FILTER parameter to NO).

Table 2 contains the information needed for the input to SE, like the number of frames stacked together to create the deep images and their seeing. It also discloses some general information, like the total number of sources detected for each band and quadrant and their limiting magnitudes at $5\sigma$, estimated from Figure 6.

### *4.1. Quality testing*

By using stellar colors and galaxy evolutionary tracks, we test our photometric accuracy in the deep UBVRI catalogue. We compare these synthetic colors to our colors, which have been derived from the convolved images aperture photometry.

Stars form a narrow sequence in most optical and near-IR color-color plots. We use the Pickles library[6] (Pickles 1998), which contains spectra of typically solar-metallicity stars, to calculate colors of stars. We do this by using the `IRAF` task `Synphot` and the filter transmission curves for VIMOS (shown in Figure 2).

Figure 7 shows eight different color-color plots for observed stars (black circles) along with colors for the Pickles library (cyan crosses) for one single quadrant. We have defined objects

[6] See http://cdsarc.u-strasbg.fr/viz-bin/ftp-index?J/PASP/110/863

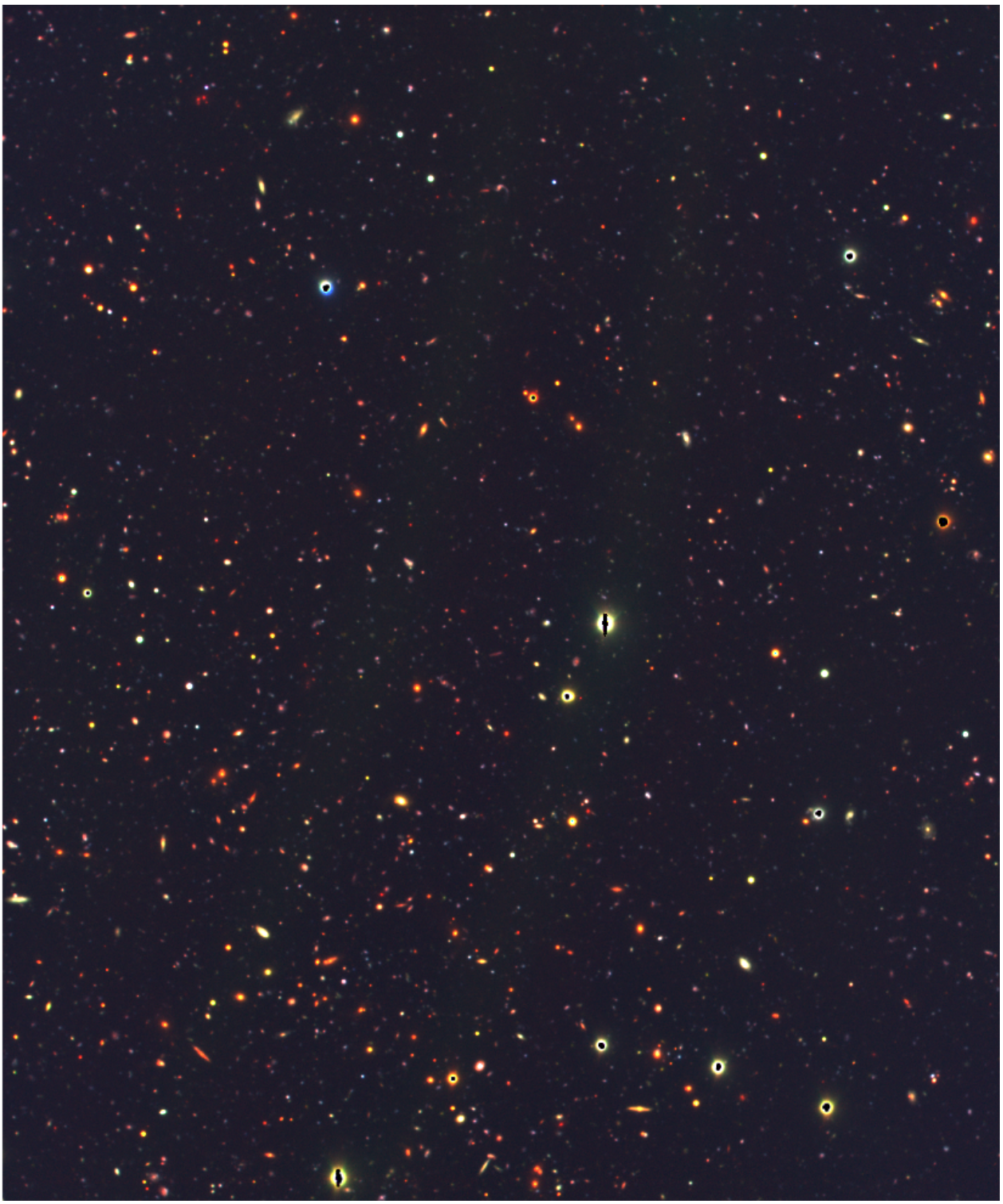

**Fig. 4.** Color composite image of the VIMOS a2 quadrant, using the I, R and V band deep images.

that are brighter in the I band than 21 and have a stellar-class parameter higher than 0.9 as stars. Any color combination of the B, V, R and I bands forms a well-defined narrow sequence, which is easy to match to the Pickles library defined sequence. But it is very hard to derive any kind of shift, or lack thereof, for the U band with only stellar tracks, since the objects do not delineate a narrow sequence. This is why together with the stellar colors, the galaxy colors and their evolutionary tracks are used to determine any possible transformation between our observed system and this standard one (for more information on the galaxy evolutionary tracks check section 7).

Figure 8 shows the same eight colors as Figure 7, again for just a single quadrant, but for galaxies instead of stars. In this case, it is easily seen that there are differences between our instrumental system and the synthetic system. To calibrate our colors, we applied the simplest possible shifts to the observed photometry in the bands where it was necessary.

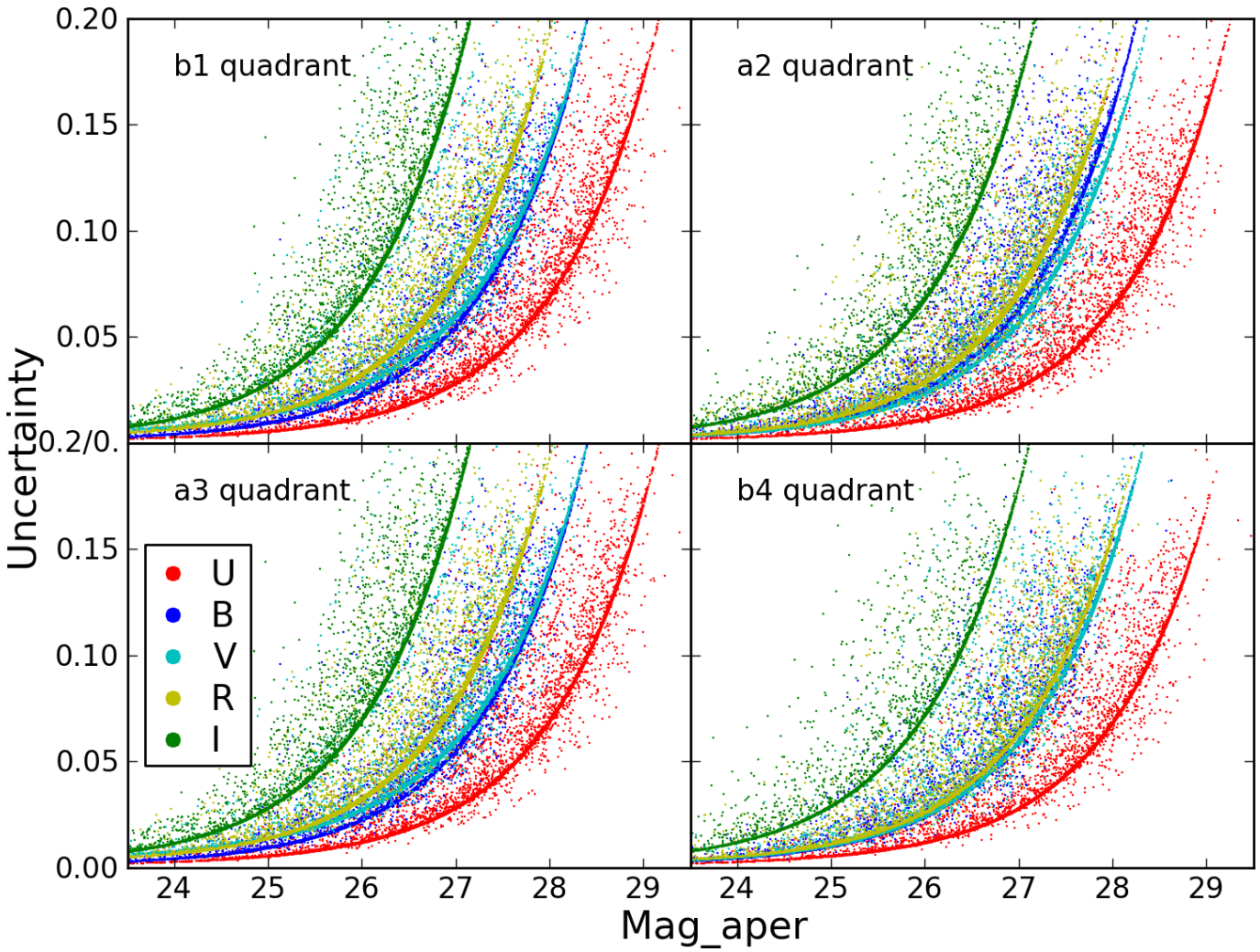


**Fig. 6.** Magnitude versus uncertainty plot for all the quadrants. These aperture magnitudes have been derived from single runs in the deep combined frames.

This consistency check was applied to each quadrant, the shifts derived from these figures are in Table 3.

It should be noted that these shifts are only applied when studying the colors of galaxies (i.e. photometric redshifts and LBGs computed from the deep I+R catalogue).

## 5. Completeness and number counts

### *5.1. Completeness*

To measure number counts, we first need to estimate our detection efficiency. We have computed our completeness by placing different kinds of artificial objects on the original deep images. Fake sources are simulated all over the original real images for a given magnitude and we recover them using SExtractor with the same input parameters used for the real detections. One thousand sources are simulated for each 0.2 magnitude bin from a magnitude of 15 to 30.

The simulated objects are a mixture of point-like and extended sources in randomized positions, since we consider that such a scenario represents a more realistic case than simulating just point-like or extended sources either in isolated or randomized positions. The fraction of each kind is determined through the FWHM parameter provided by SE. We split our catalogue into two bins, the first bin contains all detections with an aperture magnitude value between 23<mag_auto<25 and with and error below $2\sigma$, and the second bin holds all sources with a magnitude larger than mag_auto>25 and with the same error cut, error<$2\sigma$. These bins are then divided in two based on the images seeing value. Sources with a SE FWHM value larger than 2×seeing (in pixels) are considered extended sources, and sources with SE FWHM below this limit are deemed point-like. From the number of sources in each subsample we derive the fraction of sources of each kind. This process is repeated for each band. Figure 9 shows the SE FWHM distribution for the I band, for 23<mag_auto<25 in red and mag_auto>25 in grey.

These simulations were done using the `MKOBJECT` package of `IRAF`. The radius of the sources is defined differently depending on the kind of source, point-like or extended. Point-like sources have a radius given by 2×seeing, and extended sources have a radius defined by the median of the SE FWHM calculated from the sample with SE FWHM's values larger than 2×seeing.

Table 4 shows the completeness values at 90% and 50% for one of the quadrants. The first two columns correspond to values computed from simulating a mixture of point-like and extended sources in randomized positions. For comparison we also show the values computed from placing only point-like sources in randomized positions. The other quadrants behave similarly. And Figure 10 depicts the different bands completeness curves.

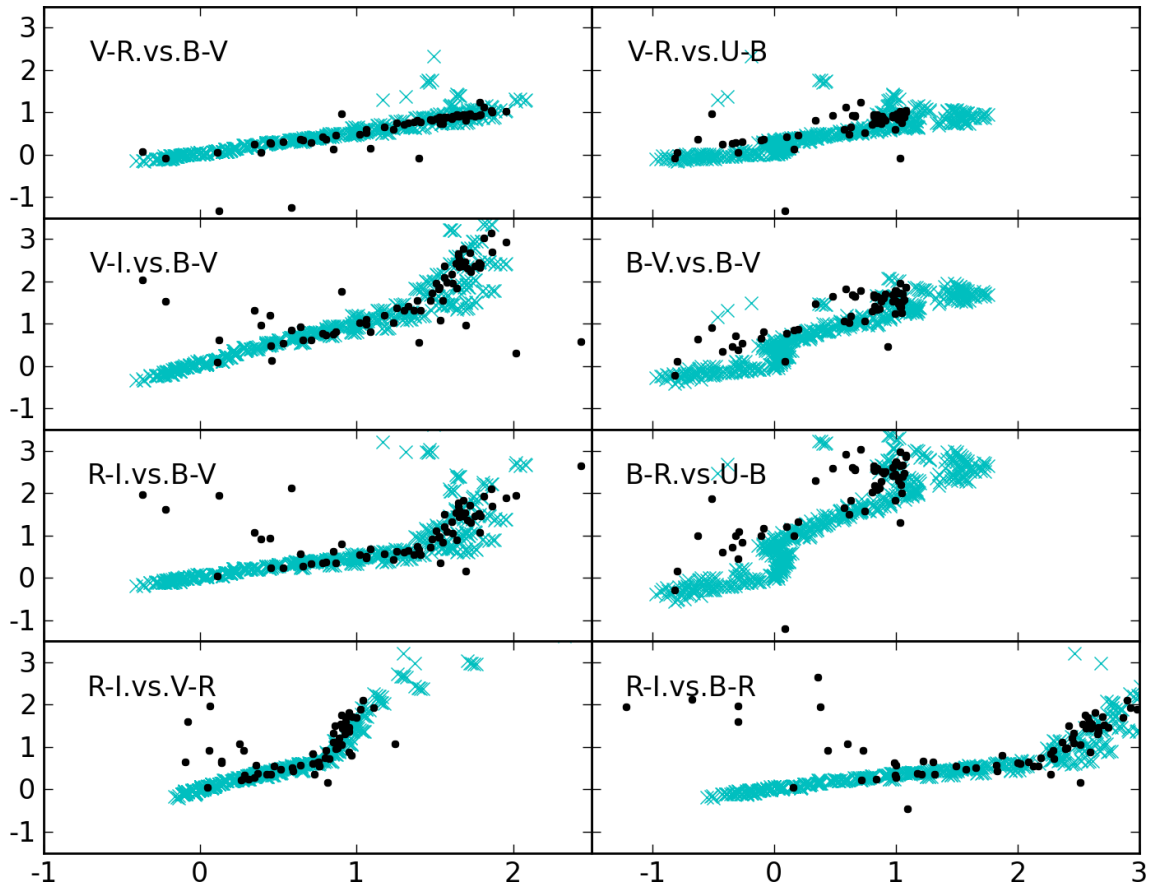


**Fig. 7.** Original star colors for one quadrant. Cyan crosses correspond to the Pickles library data. Objects classified as stars (black circle) have a class-star parameter higher than 0.9, a magnitude in the I band lower than 21 and an error in that same band below 0.1.

**Table 2.** FWHM and detection properties.

| Quadrant | Band | Total time [s] | Seeing [″] | Number of detections | Magnitude limit ($5\sigma$) |
|---|---|---|---|---|---|
| B1 | U | 31620 | 0.70 | 8285 | 28.0 |
| | B | 29580 | 0.71 | 11290 | 29.2 |
| | V | 24000 | 0.68 | 9301 | 28.4 |
| | R | 52320 | 0.64 | 10356 | 28.4 |
| | I | 114720 | 0.58 | 7605 | 27.2 |
| A2 | U | 43860 | 0.76 | 7869 | 28.2 |
| | B | 43860 | 0.69 | 10709 | 29.3 |
| | V | 23250 | 0.69 | 8500 | 28.4 |
| | R | 49440 | 0.63 | 10144 | 28.3 |
| | I | 101280 | 0.57 | 6792 | 27.2 |
| A3 | U | 29580 | 0.70 | 8141 | 28.1 |
| | B | 37740 | 0.70 | 10451 | 29.3 |
| | V | 9000 | 0.77 | 6391 | 28.1 |
| | R | 66240 | 0.67 | 10239 | 28.4 |
| | I | 112320 | 0.60 | 7583 | 27.4 |
| B4 | U | 45900 | 0.73 | 7549 | 28.3 |
| | B | 28560 | 0.73 | 9108 | 29.2 |
| | V | 24000 | 0.68 | 8457 | 28.3 |
| | R | 49920 | 0.71 | 8402 | 28.3 |
| | I | 93600 | 0.68 | 6067 | 27.1 |

**Table 3.** Derived shifts for our convolved colors by comparing them to stellar libraries and galaxy evolutionary tracks.

| | U | B | V | R | I |
|---|---|---|---|---|---|
| b1 | - | - | - | -0.08 | - |
| a2 | +0.15 | - | - | - | - |
| a3 | -0.05 | - | - | - | - |
| b4 | +0.10 | - | - | -0.15 | - |

**Table 4.** Completeness at 90% and 50% for all bands for one of the quadrants, simulating a combination of point-like and extended sources in randomized positions. The last two columns correspond to values from simulations of point-like sources placed in randomized positions.

| | Mixture | | Point-like | |
|---|---|---|---|---|
| | 90% | 50% | 90% | 50% |
| U | 23.0 | 26.3 | 24.4 | 27.0 |
| B | 23.5 | 26.9 | 27.8 | 29.1 |
| V | 23.1 | 26.5 | 27.1 | 28.3 |
| R | 22.9 | 26.4 | 27.1 | 28.3 |
| I | 22.9 | 26.4 | 24.0 | 26.6 |

### *5.2. Number counts*

We calculate the number of galaxies per square degree in each magnitude bin. First, the number of galaxies per magnitude bin was computed for each quadrant. Then, the completeness correction was applied for each quadrant. Finally, we averaged the number counts from the four quadrants to determine the final number counts, which are given in Tables 5 and 6. The second column corresponds to raw number counts and the third to corrected number counts with an associated error. The calculated errors are purely Poissonian, even if at low numbers a more correct calculation would have been to use the approximation in Gehrels (1986). Our raw number counts have been corrected for completeness and star contamination, and scaled to an area of

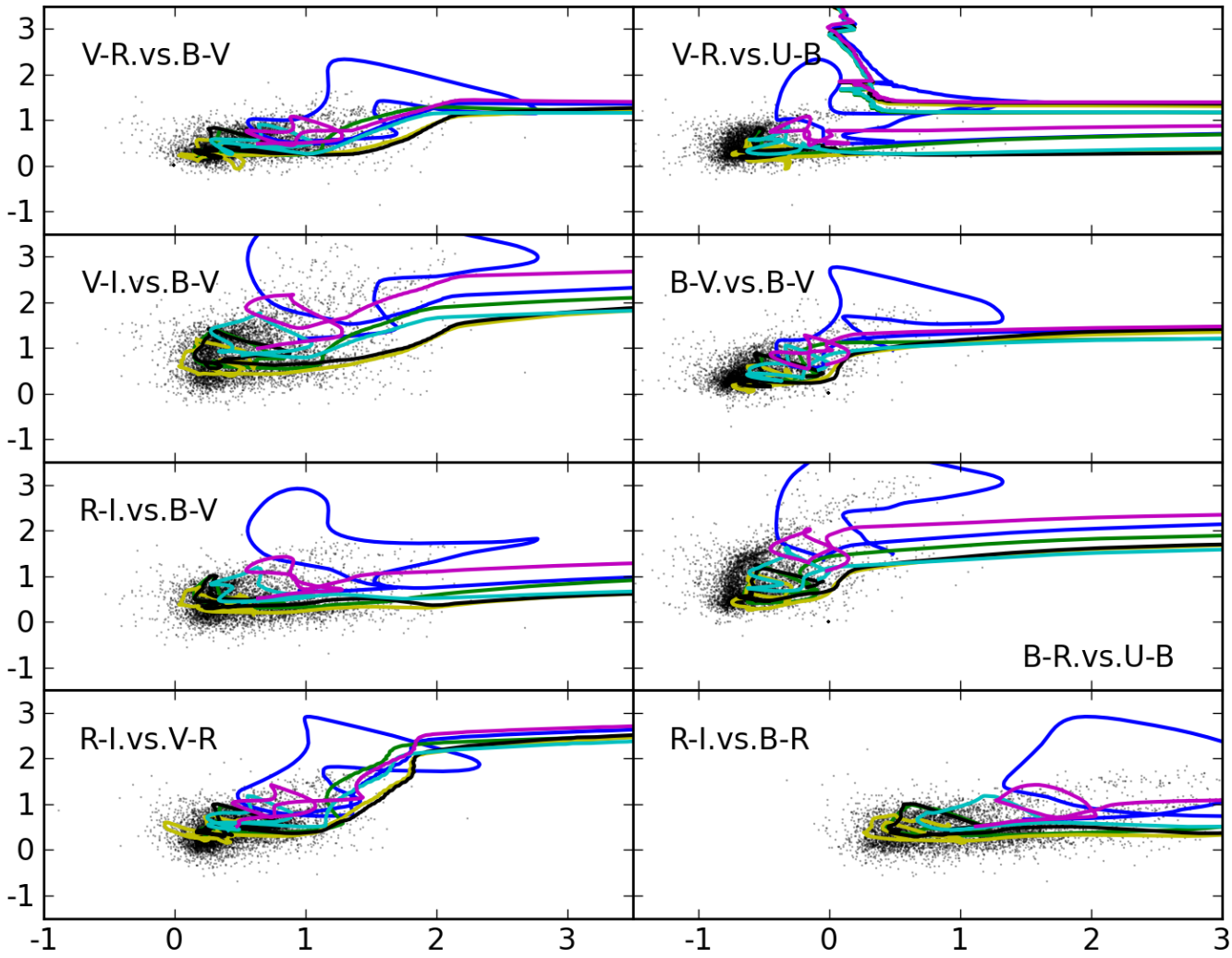


**Fig. 8.** Original galaxy colors and evolutionary tracks for one quadrant. Objects classified as galaxies have a class-star lower than 0.9, with a magnitude in the I band above 21 and its error below 0.1.

≃0.0164 deg$^2$. As we are interested in galaxy counts we need a rejection criterion for stellar sources. We use the stellarity index provided by SE and a magnitude cut to accomplish such separation. This estimate works well for fairly bright sources, but is not reliable for faint objects. Using a value of class-star>0.9 for sources with a magnitude brighter than mag_auto<22.25 we separate stars from galaxies for each band. Table 7 shows the fraction of number counts that correspond to stars in two magnitude bins, one faint (21.25<mag_auto<21.75) and one bright (24.25<mag_auto<24.75), from the total value. At a magnitude of around 22, stars still have a large effect in the number counts, but the effect becomes small at fainter magnitudes.

Note that even though we have raw number counts up to magnitude 29 or even 30, the completeness correction has not been applied at such faint magnitudes. The number of detections there is very low, therefore any completeness correction applied introduces more errors than it solves.

Figures 11 to 15 show the raw and corrected number counts as the mean of the four quadrants for U, B, V, R and I respectively. In the same plot, we also compare our number counts to those of some other surveys, see Table 8 for a description of them. The inner plot shows the different symbols used in the figure to help the identification of the surveys in the table. The error bars shown in the counts are based solely on Poisson errors.

**Table 7.** Stellar contamination measured in two magnitudes bins, one faint and one bright, derived from the stellarity index given by SExtractor. To each band the cuts in magnitude and stellarity have been applied, with mag_auto between the values defined by the chosen bin and class-star>0.9.

| | Contamination fraction | |
|---|---|---|
| | at 21.25-21.75 | at 24.25-24.75 |
| U | 0.20 | 0.07 |
| B | 0.49 | 0.07 |
| V | 0.23 | 0.04 |
| R | 0.19 | 0.05 |
| I | 0.17 | 0.06 |

The predicted stellar number counts of the galaxy at different magnitude bins are represented by the solid black line, which was derived using Besancon's model of stellar population synthesis of the galaxy (Robin et al. 2003) [7] . At faint magnitudes the stellar contamination is negligible when compared to the number of galaxies, but at bright magnitudes they dominate the number counts. Even though here we have plotted the predicted stellar number counts distribution up to magnitude 25, the galaxy num-

[7] See http://model.obs-besancon.fr/

**Table 5.** Source counts, raw and corrected for completeness, area and stellar contamination for U, B and V bands.

| Mag | U | | B | | V | |
|---|---|---|---|---|---|---|
| | N | $N_{ec}/deg^2/mag$ | N | $N_{ec}/deg^2/mag$ | N | $N_{ec}/deg^2/mag$ |
| 15.5 | - | - | - | - | - | - |
| 16.0 | - | - | - | - | - | - |
| 16.5 | - | - | - | - | 1 | 123 ± 123 |
| 17.0 | 1 | - | - | - | - | - |
| 17.5 | 4 | - | - | - | 6 | 207 ± 158 |
| 18.0 | 11 | 125 ± 125 | 3 | 185 ± 149 | 11 | 157 ± 138 |
| 18.5 | 3 | - | 10 | 154 ± 136 | 18 | - |
| 19.0 | 8 | 120 ± 120 | 15 | - | 19 | 248 ± 166 |
| 19.5 | 11 | 125 ± 125 | 11 | 124 ± 124 | 31 | 289 ± 188 |
| 20.0 | 13 | 249 ± 176 | 16 | 122 ± 122 | 47 | 566 ± 262 |
| 20.5 | 21 | 249 ± 176 | 26 | 188 ± 151 | 42 | 666 ± 289 |
| 21.0 | 52 | 1038 ± 359 | 34 | 474 ± 240 | 73 | 1409 ± 415 |
| 21.5 | 71 | 1641 ± 449 | 51 | 794 ± 316 | 119 | 2993 ± 616 |
| 22.0 | 140 | 3740 ± 692 | 83 | 1876 ± 483 | 212 | 5782 ± 868 |
| 22.5 | 282 | 9345 ± 1106 | 137 | 4359 ± 744 | 312 | 10429 ± 1180 |
| 23.0 | 511 | 17372 ± 1534 | 283 | 9196 ± 1090 | 512 | 17669 ± 1557 |
| 23.5 | 944 | 33433 ± 2171 | 545 | 18642 ± 1595 | 843 | 30340 ± 2087 |
| 24.0 | 1624 | 61153 ± 3032 | 929 | 33388 ± 2188 | 1384 | 52472 ± 2818 |
| 24.5 | 2387 | 957501 ± 3919 | 1578 | 59672 ± 3003 | 2160 | 86441 ± 3717 |
| 25.0 | 3156 | 140878 ± 5015 | 2374 | 93958 ± 3856 | 3151 | 134514 ± 4788 |
| 25.5 | 4060 | 203760 ± 6396 | 3255 | 135062 ± 4732 | 3990 | 182249 ± 5770 |
| 26.0 | 4754 | 251447 ± 7294 | 4306 | 203757 ± 6209 | 4877 | 245303 ± 7024 |
| 26.5 | 5303 | 381540 ± 10477 | 5333 | 291424 ± 7980 | 5391 | 337243 ± 9181 |
| 27.0 | 4985 | 372743 ± 10555 | 6070 | 388168 ± 9959 | 5000 | 353814 ± 9976 |
| 27.5 | 3102 | 461770 ± 16571 | 6372 | 454645 ± 11385 | 3599 | - |
| 28.0 | 468 | - | 5648 | 498976 ± 13260 | 1243 | - |
| 28.5 | 9 | - | 3926 | 535471 ± 17042 | 72 | - |
| 29.0 | 1 | - | 883 | 657236 ± 32776 | 5 | - |
| 29.5 | - | - | 40 | - | - | - |
| 30.0 | - | - | 4 | - | - | - |

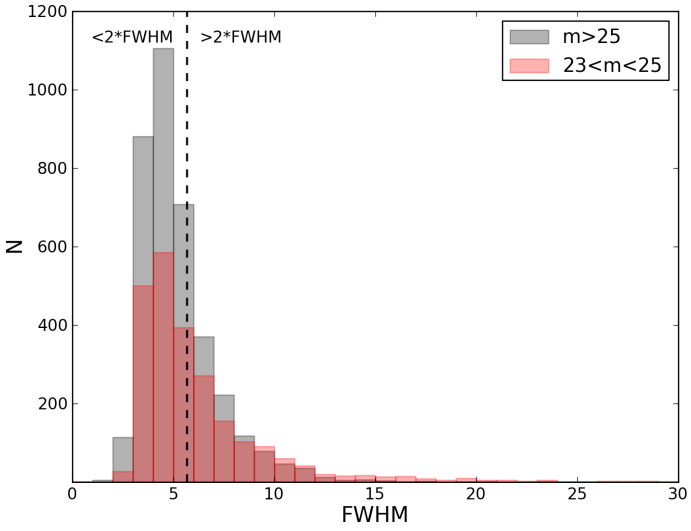


**Fig. 9.** SE FWHM parameter distribution for the I band for one quadrant. The grey histogram corresponds to sources with mag_auto>25, while the red histogram represents all sources with 23<mag_auto<25. The vertical dashed line divides both magnitude bins based on the seeing of the image.

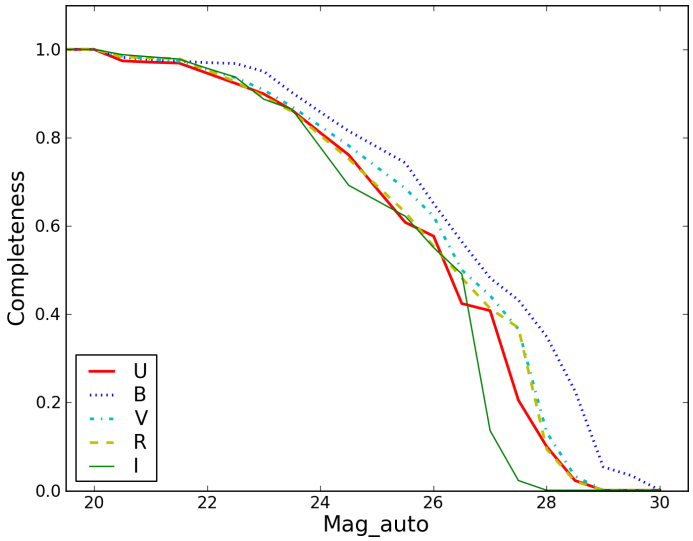


**Fig. 10.** Completeness curves for U, B, V, R and I for the a2 quadrant. The values have been computed by simulating a mix of point-like and extended sources in randomized positions.

ber counts are only corrected for stellar contamination at magnitudes m<22.25.

From the comparison of the number counts among various surveys with our data, we see that our sample is consistent with the results they produce. The observed mean values show a good agreement with them, and we are able to reproduce faintest data points from HDF observations with the HST and SDF/SXDS observations with Subaru, and for the V band also LBT observations of the Lockman Hole. At bright magnitudes, our values are based on low number of sources, which translates into large errors. This makes the number counts distribution slightly irregular, but still in agreement within the error bars with the other

**Table 6.** Source counts, raw and corrected for completeness, area and stellar contamination for R and I bands.

| Magnitude | R | | I | |
|---|---|---|---|---|
| | N | $N_{ec}/deg^2/mag$ | N | $N_{ec}/deg^2/mag$ |
| 15.5 | - | - | 2 | 126 ± 126 |
| 16.0 | - | - | 1 | 126 ± 126 |
| 16.5 | 1 | 129 ± 129 | 5 | 316 ± 198 |
| 17.0 | 4 | 166 ± 142 | 9 | 127 ± 127 |
| 17.5 | 11 | 210 ± 160 | 18 | 131 ± 131 |
| 18.0 | 12 | 126 ± 126 | 40 | 286 ± 185 |
| 18.5 | 20 | 285 ± 186 | 55 | 256 ± 177 |
| 19.0 | 43 | 378 ± 214 | 73 | 729 ± 303 |
| 19.5 | 44 | 440 ± 223 | 142 | 1405 ± 421 |
| 20.0 | 54 | 916 ± 338 | 183 | 3213 ± 637 |
| 20.5 | 99 | 2259 ± 531 | 275 | 4713 ± 775 |
| 21.0 | 176 | 4668 ± 770 | 395 | 7156 ± 961 |
| 21.5 | 211 | 5484 ± 840 | 578 | 10655 ± 1173 |
| 22.0 | 350 | 9865 ± 1140 | 739 | 17092 ± 1504 |
| 22.5 | 490 | 16692 ± 1502 | 1136 | 25059 ± 1843 |
| 23.0 | 782 | 27645 ± 1970 | 1642 | 40756 ± 2415 |
| 23.5 | 1168 | 42954 ± 2511 | 2271 | 60417 ± 2982 |
| 24.0 | 1885 | 73979 ± 3398 | 3183 | 92815 ± 3892 |
| 24.5 | 2753 | 115552 ± 4402 | 3937 | 146074 ± 5178 |
| 25.0 | 3694 | 168554 ± 5544 | 4512 | 190400 ± 6068 |
| 25.5 | 4564 | 228174 ± 6753 | 4485 | 230459 ± 6861 |
| 26.0 | 5403 | 307635 ± 8370 | 3488 | 258640 ± 7723 |
| 26.5 | 5997 | 392224 ± 10125 | 872 | 225369 ± 7606 |
| 27.0 | 5597 | 426835 ± 11395 | 1121 | 260191 ± 15270 |
| 27.5 | 4295 | 366009 ± 11140 | 28 | 38381 ± 13943 |
| 28.0 | 1405 | 467301 ± 24373 | - | - |
| 28.5 | 64 | - | - | - |
| 29.0 | 8 | - | - | - |
| 29.5 | - | - | - | - |
| 30.0 | - | - | - | - |

surveys. For the U band, only Metcalfe et al. (2001) observations of the HDF with the HST reach as deep as us. Again, for V band, we are one of the deepest surveys. Only Furusawa et al. (2008) and Kashikawa et al. (2004) with Subaru observations of SDF/SXDS and Rovilos et al. (2009) with the Lockman Hole observations with LBT reach our faint magnitudes. For B, R and I, we are also quite deep, rising up to magnitudes only achieved by HST and Subaru observations.

Discrepancies between data sets can be due to cosmic variance at the bright magnitudes, various filter systems and transmission curves used, different criterion in galaxy/point-like sources separation at intermediate fluxes, different completeness estimations and saturation effects may play a role at the brightest fluxes. It should be taken into account that some of these surveys have been corrected for different things, e.g. some do not apply completeness corrections.

## 6. Dropouts

The colors measured from different filter combinations can be used to select objects in different redshift ranges. Here we use the colors provided by the UBR, BRI, BVI, VRI and RI combinations to select galaxies that span from redshift z≃2.8 up to z≃5. U dropouts have a mean redshift of z≃3, while B dropouts have a mean value of z≃4. V and R dropouts have mean redshifts of z≃4.7 and 4.9 respectively.

The colors of detected sources were computed using an aperture radius of twice the seeing (Table 2) in the images convolved to the worst seeing (see section 4).

The colors are shown in figures 16 to 20 for one of the quadrants, along with galaxy evolutionary tracks (solid lines) and the dropout selection criteria (defined by the dashed lines). Real detections (objects detected in all three bands) are represented by black dots, whereas all sources with a dropout band magnitude fainter than its $5\sigma$ limiting magnitude value (see Table 2) are depicted with a red triangle.

The general shape of the selection criteria are chosen by comparing to other color culling cuts available in the literature. They are then adapted to our color distributions by comparing to the galaxy evolutionary tracks, so that we can avoid low redshift galaxies. We attempt to eliminate any possible contamination from stars by removing all sources with mag_auto<25 and a class-star>0.9 in the filter redward of the dropout band. We only include objects that are brighter than the $5\sigma$ values (see Table 2) in the reddest band used for each of the dropout selections. We also require the B dropouts to not be detected in U, and that R dropouts are neither detected in U nor in B. More detailed information is given in the following subsections.

### 6.1. U-dropouts

We tried different lower cuts for the U-B color (see Figure 16), from U-B≈-0.5 to 0.5 in 0.01 steps, to test the robustness of our color criteria. We modified the photometry of our catalogue in each step by adding a random shift to the source magnitude. In this way, we calculate the scatter present in our catalog, which is defined as a number of sources that have moved from their original position regarding the selection criteria (they moved from being normal galaxies to possible Lyman break galaxies or vice

**Table 8.** Number counts data found in the literature. The second column clarifies which symbol has been used, while third, fourth and fifth give technical information about the instrumentation used (telescopes, instruments and filters).

| Reference | Symbol | Telescope | Instrument | Bands |
|---|---|---|---|---|
| Alcalá et al. (2004) | ▶ | ESO/MPG 2.2m | WFI | $BVR_C$ |
| Arnouts et al. (2001) | ☆ | ESO/MPG 2.2 m CDF-S | WFI | UBVRI |
| Berta et al. (2006) | △ | ESO/MPG 2.2 m | WFI | BVR |
| Berta et al. (2008) | △ | ESO/MPG 2.2m | WFI | I |
| Capak et al. (2004) | ⋎ | Subaru | Suprime | BVRI |
| | ⋎ | KPNO | MOSAIC | U |
| Capak et al. (2007) | ⅄ | Subaru | Suprime | $i^+$ |
| Eliche-Moral et al. (2005) | + | INT | WFC | UB |
| Furusawa et al. (2008) | ◁ | Subaru | Suprime | $BVR_Ci$' |
| Grazian et al. (2009) | ◁ | LBT | LBC | U-BESSEL |
| Jeon et al. (2010) | ▼ | AZT-22 | SNUCAM | BRI |
| Kashikawa et al. (2004) | ○ | Subaru | Suprime | BVRi' |
| McCracken et al. (2003) | ⬠ | CFHT | CFH12K | BVRI |
| Metcalfe et al. (1995) | ⅄ | INT | RCA | BR |
| | ★ | WHT | Tek CCD | B |
| Metcalfe et al. (2001) | □ | HST | WFPC2 | F300W F450W F606W F814W |
| | x | HST | WFPC2 | F300W F450W F606W F814W |
| | ▲ | INT+WHT | | F450W |
| | ▷ | WHT | Tek CCD | F300W F450W F606W F814W |
| Radovich et al. (2004) | △ | ESO/MPG 2.2m | WFI | U |
| Rovilos et al. (2009) | ● | LBT | LBC | UBV |
| Smail et al. (1995) | + | Keck | LRIS | VRI |
| Volonteri et al. (2000) | ▽ | HST | WFPC2 | F300W F606W F450W F814W |
| Wilson (2003) | ★ | CFHT | UH8K | VI |
| Yasuda et al. (2001) | ◆ | SDSS telescope | SDSS imager | u'g'r'i' |

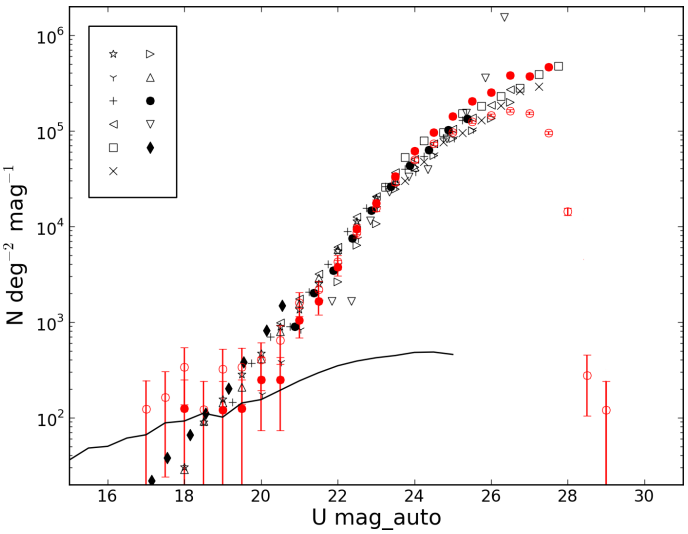


**Fig. 11.** Raw (empty red circles) and corrected for detection completeness and star contamination (solid red circles) number counts for the U band. Both values have been have been scaled to a 1 deg$^2$ area. The completeness used is derived from simulating a mix of point-like and extended sources in randomized positions all over the U band deep image. These values are compared with other major optical imaging surveys, see Table 8 for information on symbols. To clarify which surveys the number counts are being compared to, check the legend on the top left side of the figure. The black solid line corresponds to predicted stellar number counts derived from Besançon's stellar model for the galaxy, Robin et al. (2003).

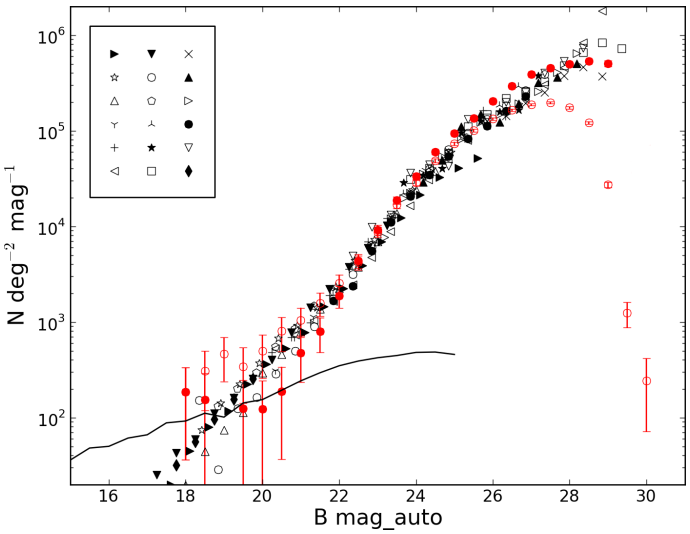


**Fig. 12.** Same as Figure 11 for the B band.

versa). The scatter is 4.1% for our current cuts, the scatter at U-B≈-0.5 and 0.5 goes up to 5.5% and 5.9% respectively.

It should be noted that this is not a measure of the contamination present in the U dropout sample. Nevertheless the scatter measurements show that our chosen cuts are the most robust with respect to the photometric error of our survey.

The U dropout selection criteria are defined by the following equations:

$$\begin{aligned} 0.4 \leq B - R &\leq 0.1 * (U - B) + 2.35 \\ U - B &\geq 0.2 * (B - R) + 0.02 \\ U - B &\leq 10 \\ U - B &\geq 1.376 * (B - R) - 1.509 \end{aligned} \quad (1)$$

A zoom-in of the possible Lyman break galaxies can be seen in Figure 21. This Figure contains the sources in all four quadrants together.

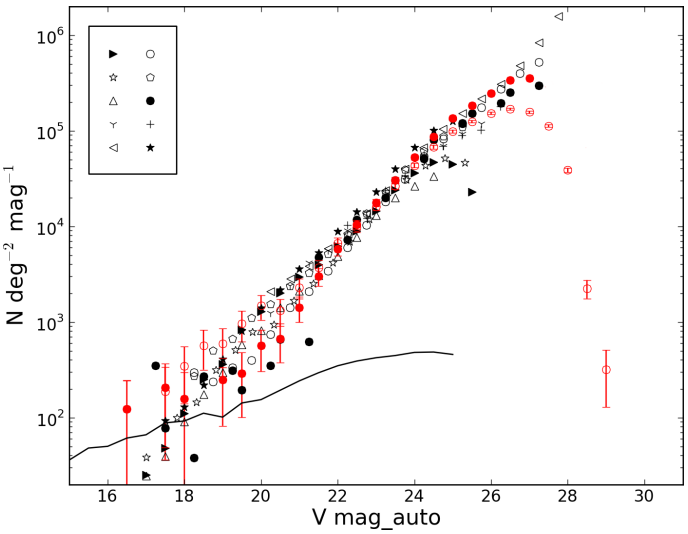


**Fig. 13.** Same as Figure 11 for the V band.

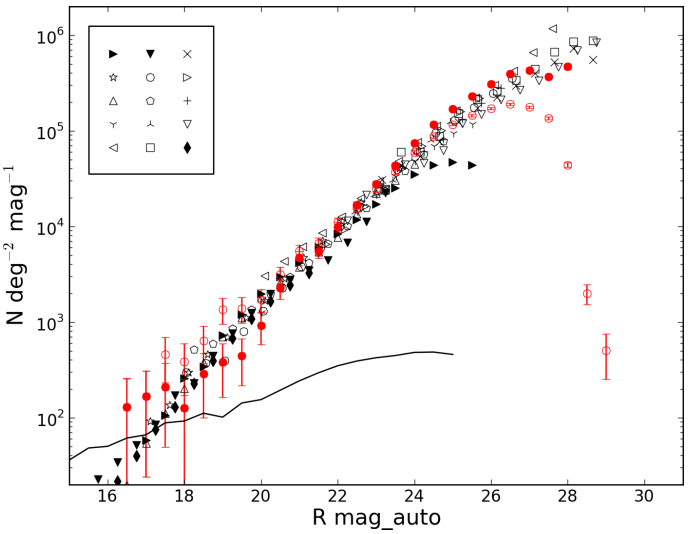


**Fig. 14.** Same as Figure 11 for the R band.

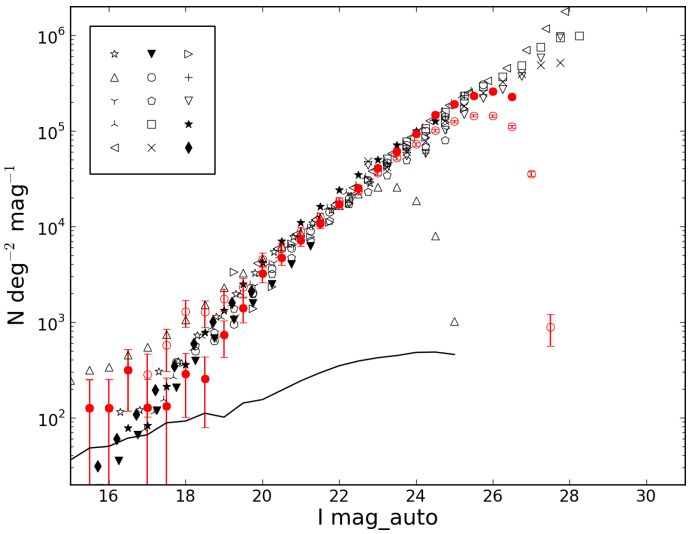


**Fig. 15.** Same as Figure 11 for the I band.

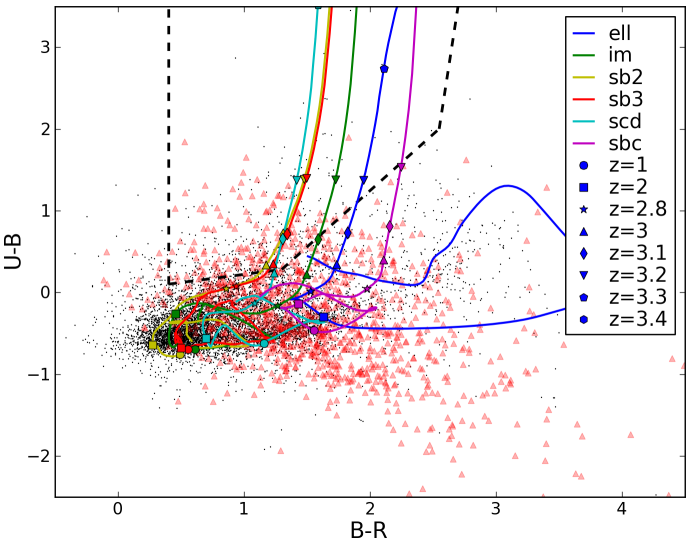


**Fig. 16.** UBR color distribution and selection criteria applied to select U dropouts for one quadrant. The solid lines correspond to the colors of different galaxy templates. The dashed lines represent our selection criteria for U dropouts. Black dots represent objects that are detected in all three bands, while red triangles represent sources undetected in the U band. For the latter we use the $5\sigma$ limiting magnitude in the U band to calculate the lower limit for the U-B clolor.

In Figure 22 we show the dropout number counts compared to measurements by other authors. As with the number counts obtained in the previous section, the dropout number counts have been first calculated individually for each quadrant, scaled to 1′ and then averaged. For R number counts, we compare our number counts to Steidel et al. (1999), who selected LBG by a $U_nG\mathcal{R}$ color combination with observations from WHT, Hale telescope and CTIO; and to Capak et al. (2004), who used KPNO-U and Subaru-B and -R filter combination. We also compare our results to those of Nonino et al. (2009), who computed them from a combination of VIMOS-U, F435W and VIMOS-R bands selected LBGs, and finally to Hildebrandt et al. (2009), with values calculated from COSMOS/CFHTLS-u and CFHTLS-g and -r culled dropouts. Our values are in agreement with the results of these authors.

### 6.2. B-dropouts

For the BRI color-color plots we compare two different cuts, the same cut used by Capak et al. (2004) and by Ouchi et al. (2004), hereafter Capak04 and Ouchi04 respectively. The cuts have been slightly modified so they fit better our data and the evolutionary tracks used. The magnitude cut for these dropouts is done in the R band for Capak04's cut but in the I band for Ouchi04's. In both cases we used their 5 $\sigma$ value (check Table 2).

We also selected B dropouts using a BVI color combination. The BVI cut is based on our Capak04's BRI cut, mainly the cut on the B-R axis, so we are selecting sources with almost the same redshift but avoiding the lower redshift regions as defined by the galaxy tracks.

The B dropout selection criteria are defined by the following equations:

– for the BRI color combination:

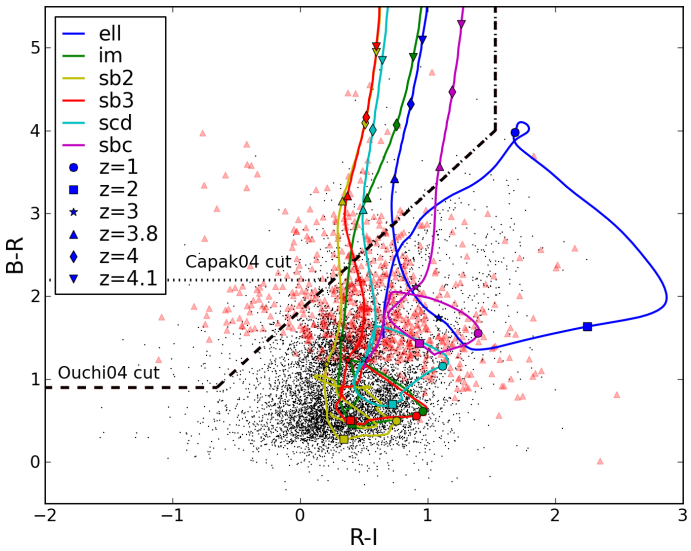


**Fig. 17.** As Figure 16 but using the BRI combination to select B dropouts. Dotted lines define the selection criteria based on Capak04's cuts, while dashed lines correspond to Ouchi04's cuts.

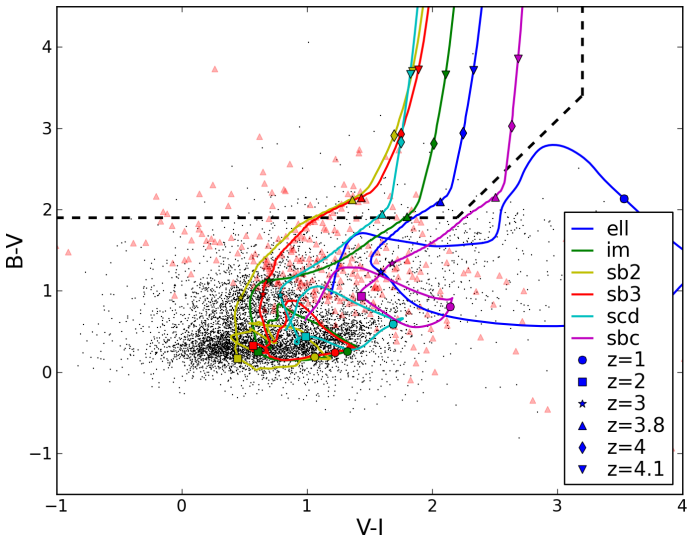


**Fig. 18.** As Figure 16 but using the BVI combination to select B dropouts.

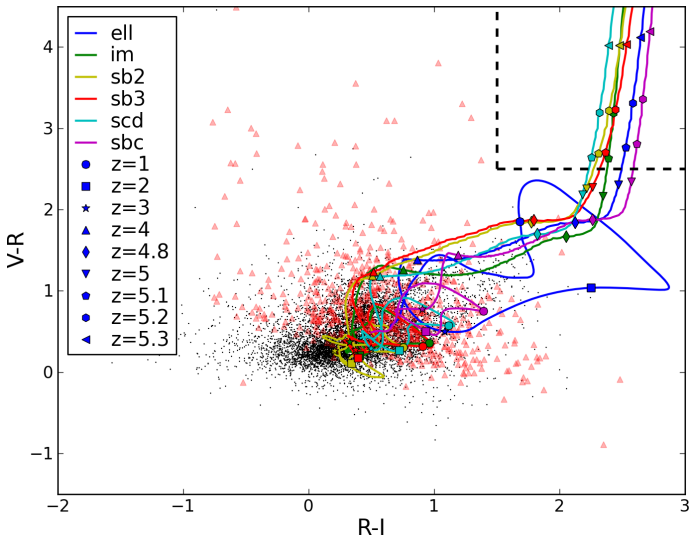


**Fig. 19.** As Figure 16 but using the VRI combination to select V dropouts.

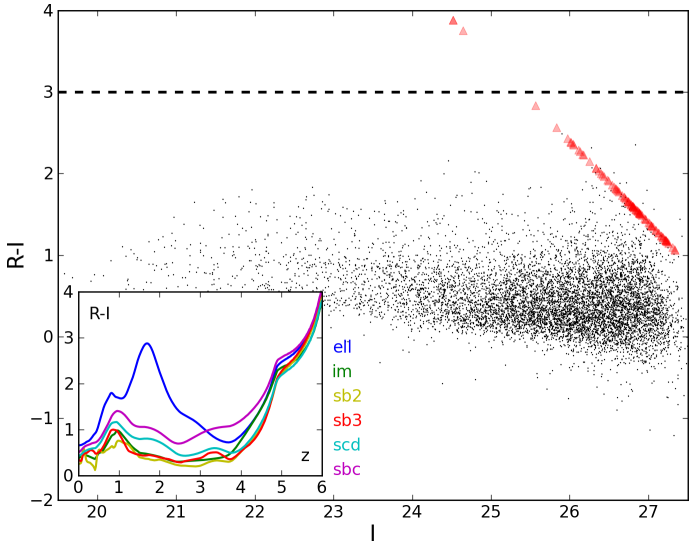


**Fig. 20.** RI color distribution and selection criteria applied to select R dropouts. This plot contains all the sources of the four quadrants. The inside plot shows the variation of the R-I color of the galaxy evolutionary tracks with redshift.

1. Capak04's cut:

$$\begin{aligned} -10 \leq R - I \leq 1.53 \\ B - R \leq 10 \\ B - R \geq 2.2 \\ B - R \geq 1.406 * (R - I) + 1.848 \end{aligned} \quad (2)$$

2. Ouchi04's cut:

$$\begin{aligned} -10 \leq R - I \leq 1.53 \\ B - R \leq 10 \\ B - R \geq 0.9 \\ B - R \geq 1.422 * (R - I) + 1.824 \end{aligned} \quad (3)$$

– for the BVI color combination:

$$\begin{aligned} -5 \leq V - I \leq 3.2 \\ B - V \leq 10 \\ B - V \geq 2 \\ B - V \geq 1.4 * (V - I) - 1.08 \end{aligned} \quad (4)$$

In figure 23 we show the color distribution of the B dropouts for one of the quadrants. Squares represent B dropouts selected using a BVI combination of colors, with shadow squares depicting sources with B band upper limits. Dots and triangles indicate B dropouts chosen with a BRI combination of colors, with cyan color for sources picked up by the cut similar to Ouchi04's, and black to represent a more conservative cut, defined by Capak04's. Dots correspond to sources with real detection in all three bands, while sources with no detection in the B band are symbolized by triangles. For the latter, as well as for the shadow squares, we use the $5\sigma$ limiting magnitude to calculate a

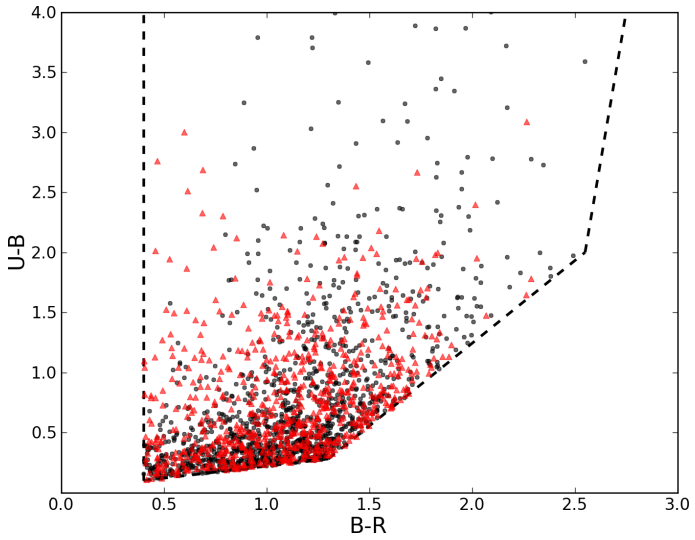


**Fig. 21.** Zoom in of the UBR culling selection for all quadrants together.

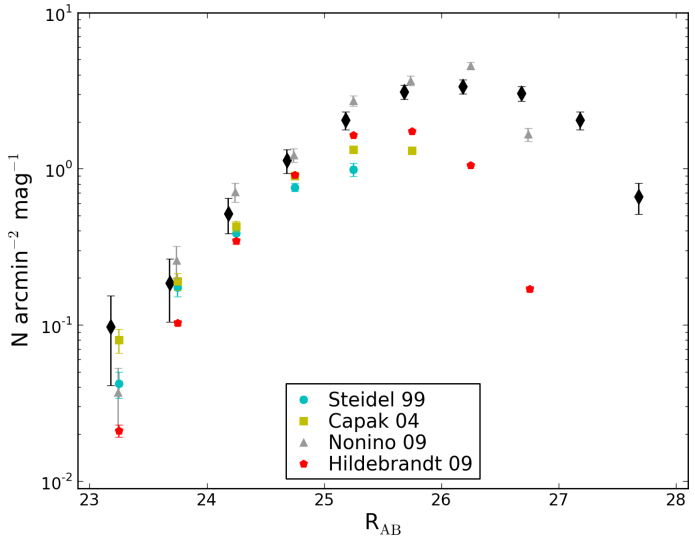


**Fig. 22.** Raw number counts of U dropouts uncorrected for incompleteness or contamination other than stars at bright magnitudes, compared to other measurements from the literature. The error bars in Capak et al. (2004) (yellow square) and Nonino et al. (2009) (grey triangle) are 1 $\sigma$ Poisson fluctuations, while the errors in Steidel et al. (1999) (cyan circle) are corrected for interlopers and include an estimate of cosmic variance. Also compared to Hildebrandt et al. (2009) (red pentagon).

lower limit for B-R and B-V. This plot shows the selected Lyman break galaxies for one quadrant. From the plots we can see that our Ouchi04's BRI cut selects more sources than Capak04's BRI cut, but most of the sources selected by the last cut are contained in the former, which is expected. If we compare BRI and BVI cuts, we see that they do select not exactly the same sources, just a large fraction of them. The BRI combination of filters selects a larger number of sources and their redshift distribution is not exactly the same as with the BVI combination, see subsection 6.1.

Figure 24 shows the different number counts detected by using the three different cuts. Black diamonds and red squares select B dropouts using the same filters, BRI, with the difference that the black diamonds have been selected using Ouchi04's cut and red squares using Capak04's, while cyan circles select B dropouts using the BVI color combination. The overall shape of the distribution is the same for the different B dropout selection criteria, with Ouchi04's cut derived values being higher that for the other two selecting options, and with BRI color combination reaching deeper than BVI.

We compared our I number count values to other authors in Figure 25. Steidel et al. (1999) used the two color diagram of WHT/Hale telescope/CTIO G-$\mathcal{R}$ versus $\mathcal{R}$-I to select B dropouts; Metcalfe et al. (2001) derived number counts of LBGs chosen by the two color diagram F450W-F606W versus F606W-F814W with observations on the WHT and HST; Capak et al. (2004) and Ouchi et al. (2004) calculated them with the Subaru BRI filter combination. Hildebrandt et al. (2009) derived the number counts of LBGs from CFHTLS g-r versus r-i. Our values are in agreement with these other authors within the error bars, but we do not reach as deep as Hildebrandt et al. (2009) nor as Ouchi et al. (2004).

### 6.3. V-dropouts

The VRI selection criteria for V dropouts are arbitrarily chosen, since there are no other culls to compare with in the literature. The cuts are chosen based on the galaxy tracks, to avoid low redshift contamination, and should provide dropouts at z≳5.

The V dropout selection criteria are defined by the following equations:

$$1.5 \leq R - I \leq 10$$
$$2.5 \leq V - R \leq 3.5 \quad (5)$$

### 6.4. R-dropouts

For the R dropouts, see Figure 20, the cut at R-I = 3 is defined solely based in the galaxy evolutionary tracks plotted in the small panel. At this cut, we are rejecting all lower redshift sources while still picking sources with redshift≥5. We cull 5 sources applying this selection criteria, with magnitudes in the I band mag_aper≃24.5-2.5.

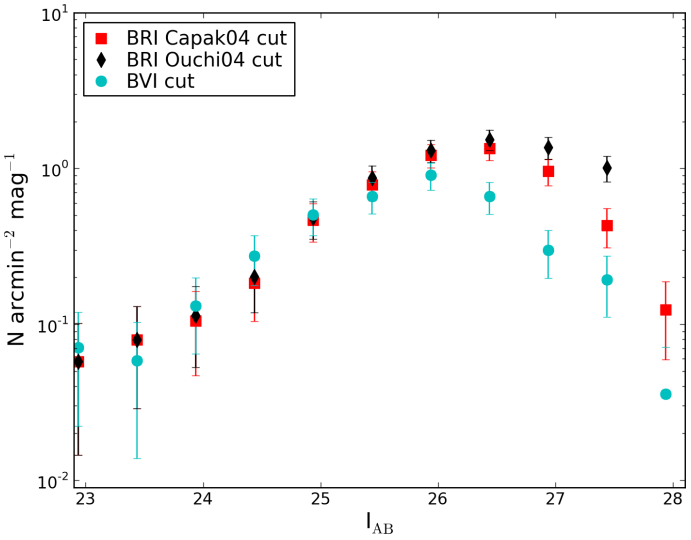


**Fig. 24.** Comparison between different selection criteria for B dropouts. Black diamonds represent raw number counts calculated from Lyman break galaxies selected with Ouchi04's BRI selection criteria, red squares are raw number counts for Capak04's BRI cut and cyan circles correspond to values calculated from BVI selected sources.

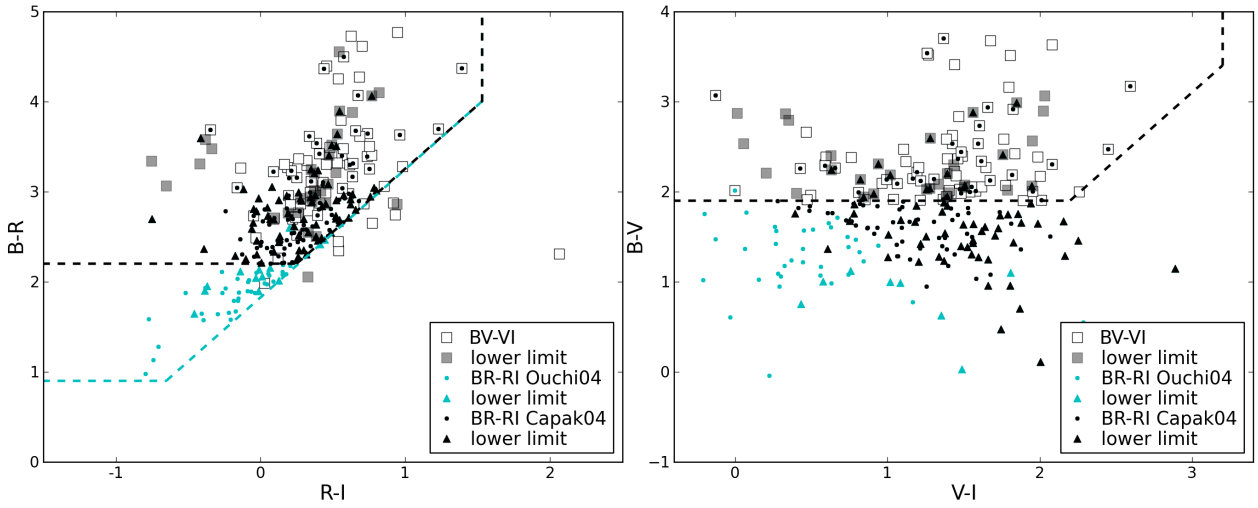


**Fig. 23.** Left panel: BRI color plot for B dropouts selected with three different criteria. Right panel: BVI color plot for B dropouts. Squares represent B dropouts selected using a BVI combination of colors, with shadow squares depicting sources with no real B band detection. Dots and triangles indicate B dropouts chosen with a BRI combination of colors, with cyan for sources picked up by Capak04's cut, and black to represent a more conservative cut, better suited to our colors and evolutionary tracks.

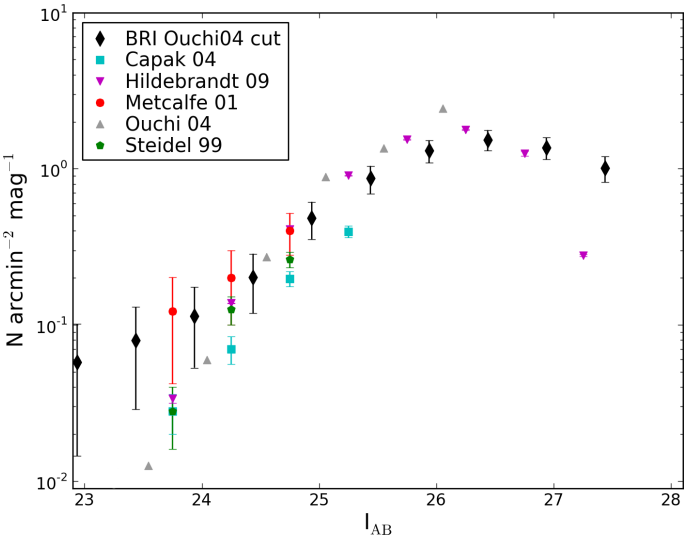


**Fig. 25.** Raw number counts of B dropouts selected using the BRI combination of colors, uncorrected for incompleteness or contamination other than stars at bright magnitudes. These values are compared to Capak et al. (2004) (cyan square), Hildebrandt et al. (2009) (magenta inverted triangle), Metcalfe et al. (2001) (red cicle) and Ouchi et al. (2004) (grey triangle) and Steidel et al. (1999) (green pentagon).

### *6.5. Photometric redshifts for dropout selected galaxies*

The distributions of photometric redshifts for the dropout selected galaxies are presented in Figure 26. We explain how these redshifts have been calculated in the next section. The top panel shows the U dropout redshift distribution, with a mean value of z≃3. The second, third and fourth panel show the redshift distribution of B dropouts selected using the three different cuts. The first of these two plots are LBGs culled by the two color combination given by BRI, while the last one displays LBGs selected through a BVI color combination. Using the culls defined by BRI instead of BVI provides a larger LGB sample and reduces the number of low redshift interlopers. Capak04's and Ouchi04's cuts have a similar redshift distribution and fraction of contaminants, 19.9% and 20.3% respectively. A BVI cull detects ≃40% less sources than Ouchi04's cut, while increasing the number of contaminants by 7%. The three different cuts have similar redshifts distributions, with a mean value of z≃3.68 if we ignore the contamination at lower redshifts. In our case, the V dropouts are very sparse, and none of them have a computed redshift.

an der BurgVAN DER BURG et al. (2010) discuss the contamination fraction of stars and low redshift galaxies in their dropout samples. They have u, g and r observations of the CFHT Legacy Survey Deep fields. Stellar contamination is zero or negligible at bright magnitudes, since selection culls steer away from the stellar tracks, and is only important at faint magnitudes for r and i bands due to photometric scatter. The contamination from low redshift galaxies is in general higher than the stellar one and affects both faint and bright magnitudes for g dropouts. U dropouts are free of low redshift sources contamination, since the Lyman break for galaxies at z≃3 is still blue-ward of the z≃0 Balmer/4000Å break. This is certainly not the case for higher redshifts, so B dropouts suffer from a significant contamination at the bright end.

Note that sources with a low redshift value can not be immediately rejected as a Lyman break galaxy. Sources may have a multi-peaked or a broad probability distribution, making it difficult to find an accurate photometric redshift.

The redshifts for V and R dropouts are not determined due to the lack of bands with proper photometry, but they are candidates for high redshift galaxies.

## 7. Photometric redshifts

We use the GOODZ code (Dahlen et al. 2010) to calculate photometric redshifts for objects present in the photometric redshift catalog. This is a template fitting code using 16 spectral energy distributions created from interpolating four templates (ell, scd, sbc, im) from Coleman et al. (1980) and two templates (sb2, sb3) from Kinney et al. (1996). These templates cover a spectral type range from early type ellipticals to late starbursts. The code uses an absolute V band luminosity prior and requires that an object is detected in at least three filters to calculate the photometric

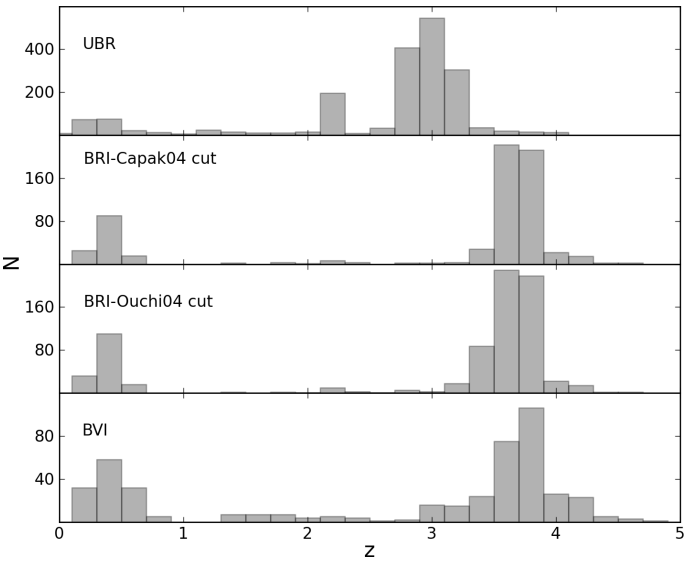


**Fig. 26.** Distribution of photometric redshifts for objects selected as Lyman break galaxies for the different applied selecting cuts. First panel shows U dropouts selected using the UBR color combination. Second to last panel display the B dropouts using BRI Capak04's cut, Ouchi04's cut and finally BVI selection criteria.

redshift. The fitting is then done using a $\chi^2$-technique, where:

$$\chi^2(t, z, m_\alpha) = \sum_i \frac{(m_i - (T_i(t, z) + m_\alpha))^2}{\sigma_i^2} \quad (6)$$

is minimized. Here $m_i$ and $\sigma_i$ are the observed magnitudes and uncertainties in filter $i$, respectively. $T_i(t, z)$ is the magnitude in the $i$–filter of template $t$, redshifted to $z$. This magnitude is derived by convolving the filter curve and the quantum efficiency of the detector with the galaxy template. The quantity $m_\alpha$ is a normalization constant corresponding to the luminosity of the template galaxy.

### 7.1. Calibration with spectroscopic redshifts of HDF-S

Due to the lack of spectroscopic redshifts in the ELAIS-S field, we used data from another survey taken with the same telescope and filters as our data and with available spectroscopic redshifts, to estimate the accuracy of the photometric redshifts and to calibrate the technique. Checking the archive data we found that the Hubble Deep Field south had been observed with VIMOS U, B, V, R and I filters. We use available spectroscopic redshifts from Glazebrook et al. (2006), Rigopoulou et al. (2005), Sawicki & Mallén-Ornelas (2003) and Vanzella et al. (2002), producing a total of 217 sources with spectroscopic redshifts (after rejecting sources with unknown or equal to zero redshift). Since they target the same field some sources are observed various times and some are outside of the VIMOS HDF-S field, hence we reject them. On the other hand several sources are detected multiple times due to field of view being divided in four quadrants. This makes that in practice we have 475 sources with spectroscopic redsfhit.

We treated this data using the same process as our data, including reduction, calibration, alignment, astrometry and source detection. With these calibrated data and using the photometric redshift code we calculated photometric redshifts. We altered the code's input parameters to optimize the output values. This includes adding a correction to the photometry in the different bands to account for possible systematic errors in e.g., the photometric zero points or the tabulated filter transmission functions. We compare different sets of photometric redshifts computed with different input parameters to the spectroscopic redshifts, until we found the best possible distribution. This is estimated by the scatter ($\sigma_z = rms(dz)$, with $dz = (z_{spec} - z_{phot})/(1 + z_{spec})$) and fraction of outliers determined from the comparisons.

Table 9 shows the different scatter and fraction of outliers values when using the spectroscopic redshift calibration and/or the photometric transformations. The last line is for the values restricted to $z_{spec} \leq 1.5$. While the scatter value is fairly similar to that of the whole sample, there is a slight improvement in the fraction of outliers when applying this condition, it goes down to 7.6%.

Figure 28 shows the relation between photometric and spectroscopic redshifts. The solid line indicates $z_{phot} = z_{spec}$, and the red dashed lines represent relations of $z_{phot} = z_{spec} \pm 0.3 \times (1 + z_{spec})$. This is the relation used to define the outliers, any sources falling outside this limits is considered a catastrophic failure. The lower Figure shows the relation $dz = (z_{spec} - z_{phot})/(1 + z_{spec})$ with the spectroscopic redshift, with the same lines as the upper one. With this constraints we measure a 9.2% of outliers in our spectroscopic sample with an accuracy of $\sigma_z$=0.085

The distribution of the derived photometric redshifts is shown in Figure 27 and overplotted in grey we can see the spectroscopic redshifts' distribution. There is a redistribution of redshifts as can be seen from the different lengths of the bins, but both redshifts, photometric and spectroscopic, have a median value of ≃0.5.

### 7.2. SVISS photometric redshifts

With the spectroscopic redshifts calibrations, calculated in the previous subsection, and the color transformations, determined in section 6, we compute the photometric redshift values for our data.

Figure 29 shows the redshift distribution of the whole sample with I_err<0.5 divided by magnitude intervals.

## 8. Summary and conclusions.

This paper describes the work done to create a catalogue from deep UBVR and I imaging data of a portion of the ELAIS-S1 field. We have also computed number counts, identified Lyman break galaxies and derived number counts for U and B dropouts, and calculated the photometric redshifts for the sources in the catalogue.

Here, we summarize the main results:

1. We present a photometrically and astronomically calibrated set of images, with measured mean limiting magnitudes at 5$\sigma$ of U=28.15, B=29.25, V=28.3, R=28.35 and I=27.22 in

**Table 9.** Scatter and fraction of outliers for photometric redshifts applying the derived color shifts in section 4.3 and/or the computed values from comparing them to spectroscopic redshifts. These values are the mean computed for the four quadrants.

| $z_{spec}$ calibration | Color shifts | $\sigma_z$ | Fraction of outliers |
|---|---|---|---|
| NO | NO | 0.091 | 0.11 |
| YES | NO | 0.095 | 0.10 |
| YES | YES | 0.085 | 0.092 |
| YES ($z_{spec} \leq 1.5$) | YES | 0.082 | 0.076 |

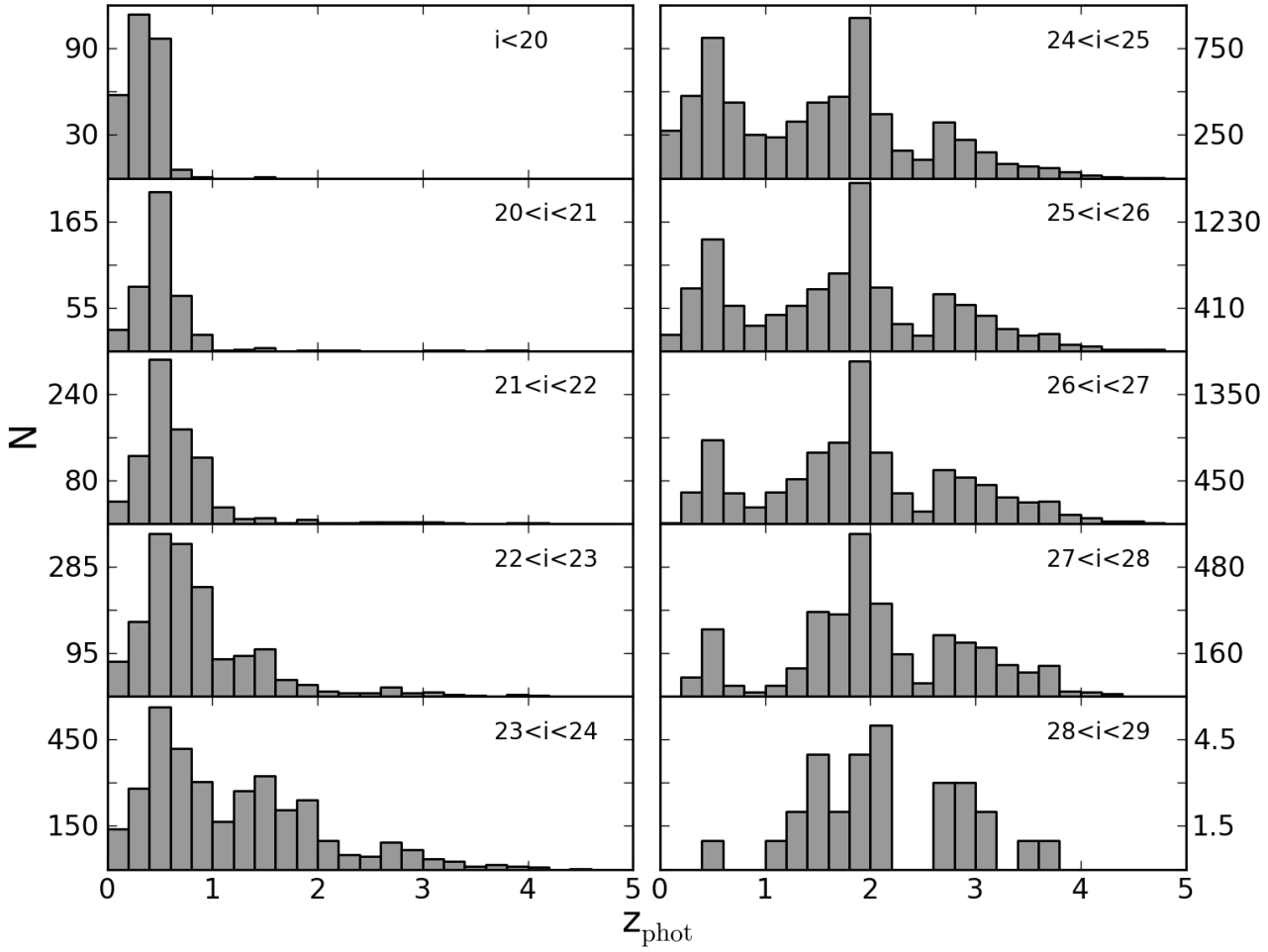


**Fig. 29.** Photometric redshift distribution for the ELAIS data, with all quadrants joined together divided by magnitude interval.

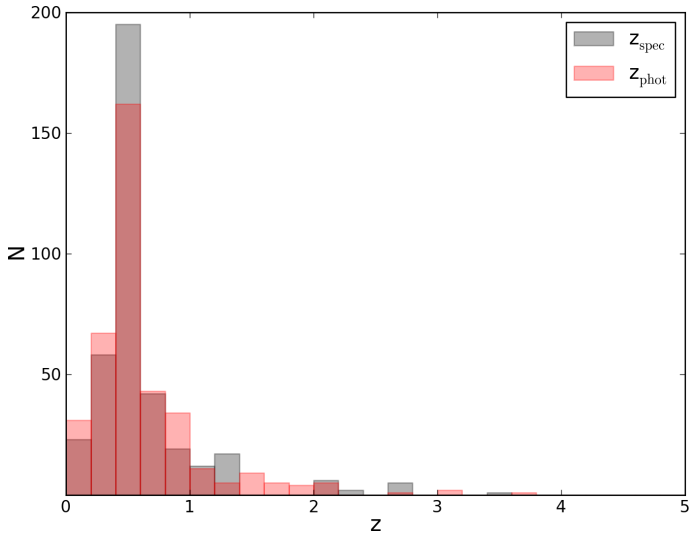


**Fig. 27.** Histogram showing the distribution of redshifts. The red histogram shows the distribution of photometric redshifts while the grey region shows their spectroscopic counterparts.

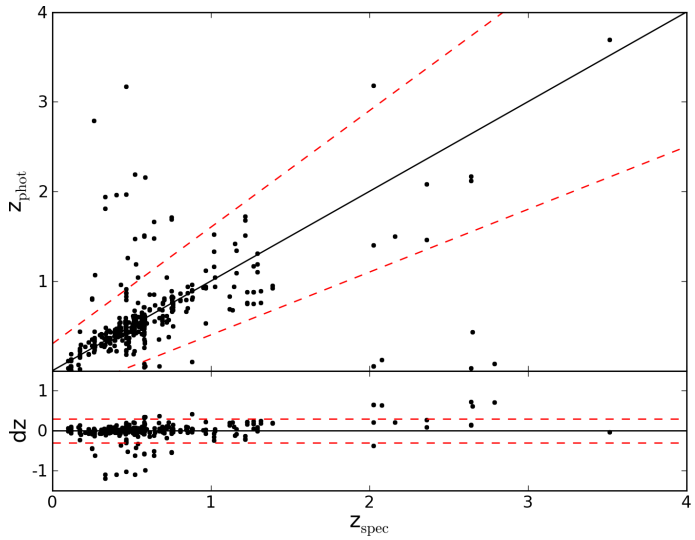


**Fig. 28.** Comparison of the photometric and spectroscopic redshifts for the HDF-S. Lower panel shows the difference between these redshifts $dz = (z_{spec} - z_{phot})/(1 + z_{spec})$. Solid lines indicate $z_{phot} = z_{spec}$, and red dashed lines represent relations of $z_{phot} = z_{spec} \pm 0.3 \times (1 + z_{spec})$.

the Vega system. The total number of sources contained in the catalogues is ~50000 and ~35000 for the deep UBVRI and deep I+R catalogues respectively.

2. Before combining the single science frames, we weighted them by the seeing, increasing the number of detections

by 10% and reducing the magnitude errors by 12.5% in the faintest magnitudes compared to a combination without weighting.

3. From the comparison with stellar libraries and galaxy tracks we notice that there are differences between our observed system and the synthetic one, therefore, to keep the consistency between both systems we apply shifts to our magnitudes: U+0.15 for the a2 quadrant, U-0.05 for a3, for b1 R-0.08 and for b4, U+0.1 and R-0.15.
4. The detection efficiency as a function of magnitude is estimated by adding fake sources into our real images. We placed a mixture of point-like and extended sources in randomized positions, with their ratio determined as a function of the SExtractor `FWHM` parameter.
5. The number counts determined as the mean of the four quadrants are consistent with those of other surveys after applying completeness correction. They are also corrected for stellar contamination and an estimate of its effect is derived from Besançon's model of stellar population synthesis of the Galaxy. We are able to reproduce the faintest data points from HDF observations with the HST for UBR and I. For V band number counts we reach as deep as SDF/SXDS observations with Subaru and Lockman Hole observations with LBT.
6. Lyman break galaxies are selected through the combination of colors UBR, BRI, BVI and VRI. R raw number counts for U dropouts agree with other literature values available. We compare different cuts for B dropouts, we use Capak04's and Ouchi04's BRI cut and BVI color combination. BRI and BVI cuts do not select the same sources, not only in number but also different sources. When compared with other literature values, they agree within the error bars, although the values at brighter magnitudes are lower. U dropouts have mean photometric redshift value of <z>$\sim$ 3 and B dropouts of <z>$\sim$ 3.7. V dropouts on the other hand are very few, and they do not have available photometric redshifts.
7. Photometric redshifts are calculated using the GOODZ code (Dahlen et al. 2010), which is based on the template fitting technique. The photometric redshifts have been calibrated using HDF-S observations with VIMOS, achieving an accuracy of $\sigma_z$=0.085 with 9.2% fraction of outliers, with the appliance of the color transformations together with the spectroscopic redshift calibrations.

This data set is among the deepest available from ground-based observations. Our reduced and stacked images are reachable at ... and source catalogs are online in ....

## References


Abdalla, F. B., Banerji, M., Lahav, O., & Rashkov, V. 2008, ArXiv e-prints
Alcalá, J. M., Pannella, M., Puddu, E., et al. 2004, A&A, 428, 339
Arnouts, S., Vandame, B., Benoist, C., et al. 2001, A&A, 379, 740
Baum, W. A. 1962, in IAU Symposium, Vol. 15, Problems of Extra-Galactic Research, ed. G. C. McVittie, 390–+
Bell, E. F., McIntosh, D. H., Katz, N., & Weinberg, M. D. 2003, ApJS, 149, 289
Benítez, N. 2000, ApJ, 536, 571
Berta, S., Rubele, S., Franceschini, A., et al. 2006, A&A, 451, 881
Berta, S., Rubele, S., Franceschini, A., et al. 2008, VizieR Online Data Catalog, 348, 80533
Bertin, E. & Arnouts, S. 1996, A&AS, 117, 393
Bolzonella, M., Miralles, J., & Pelló, R. 2000, A&A, 363, 476
Brown, G. S. & Tinsley, B. M. 1974, ApJ, 194, 555
Capak, P., Aussel, H., Ajiki, M., et al. 2007, ApJS, 172, 99
Capak, P., Cowie, L. L., Hu, E. M., et al. 2004, AJ, 127, 180
Christlein, D., Gawiser, E., Marchesini, D., & Padilla, N. 2009, MNRAS, 400, 429
Coleman, G. D., Wu, C., & Weedman, D. W. 1980, ApJS, 43, 393
Collister, A. A. & Lahav, O. 2004, PASP, 116, 345
Connolly, A. J., Csabai, I., Szalay, A. S., et al. 1995, AJ, 110, 2655
Dahlen, T., Mobasher, B., Dickinson, M., et al. 2010, ApJ, 724, 425
Dahlen, T., Mobasher, B., Somerville, R. S., et al. 2005, ApJ, 631, 126
Eliche-Moral, C., Balcells, M., Prieto, M., & Cristóbal-Hornillos, D. 2005, in Revista Mexicana de Astronomia y Astrofisica, vol. 27, Vol. 24, Revista Mexicana de Astronomia y Astrofisica Conference Series, ed. A. M. Hidalgo-Gámez, J. J. González, J. M. Rodríguez Espinosa, & S. Torres-Peimbert, 237–238
Faber, S. M., Willmer, C. N. A., Wolf, C., et al. 2007, ApJ, 665, 265
Feldmann, R., Carollo, C. M., Porciani, C., et al. 2006, MNRAS, 372, 565
Furusawa, H., Kosugi, G., Akiyama, M., et al. 2008, ApJS, 176, 1
Gabasch, A., Bender, R., Seitz, S., et al. 2004, A&A, 421, 41
Gabasch, A., Goranova, Y., Hopp, U., Noll, S., & Pannella, M. 2008, MNRAS, 383, 1319
Gawiser, E., van Dokkum, P. G., Herrera, D., et al. 2006, ApJS, 162, 1
Gehrels, N. 1986, ApJ, 303, 336
Giacconi, R., Rosati, P., Tozzi, P., et al. 2001, ApJ, 551, 624
Giavalisco, M. 2002, ARA&A, 40, 579
Giavalisco, M., Ferguson, H. C., Koekemoer, A. M., et al. 2004, ApJ, 600, L93
Glazebrook, K., Verma, A., Boyle, B., et al. 2006, AJ, 131, 2383
Gooch, R. 1996, in Astronomical Society of the Pacific Conference Series, Vol. 101, Astronomical Data Analysis Software and Systems V, ed. G. H. Jacoby & J. Barnes, 80–+
Grazian, A., Menci, N., Giallongo, E., et al. 2009, A&A, 505, 1041
Hansen, S. M., McKay, T. A., Wechsler, R. H., et al. 2005, ApJ, 633, 122
Heidt, J., Appenzeller, I., Gabasch, A., et al. 2003, A&A, 398, 49
Hildebrandt, H., van Waerbeke, L., & Erben, T. 2009, A&A, 507, 683
Hsieh, B. C., Yee, H. K. C., Lin, H., & Gladders, M. D. 2005, ApJS, 158, 161
Jeon, Y., Im, M., Ibrahimov, M., et al. 2010, ApJS, 190, 166
Kashikawa, N., Shimasaku, K., Yasuda, N., et al. 2004, PASJ, 56, 1011
Kashikawa, N., Yoshida, M., Shimasaku, K., et al. 2006, ApJ, 637, 631
Kinney, A. L., Calzetti, D., Bohlin, R. C., et al. 1996, ApJ, 467, 38
La Franca, F., Gruppioni, C., Matute, I., et al. 2004, AJ, 127, 3075
Landolt, A. U. 1992, AJ, 104, 340
Le Fèvre, O., Mellier, Y., McCracken, H. J., et al. 2004, A&A, 417, 839
Le Fèvre, O., Saisse, M., Mancini, D., et al. 2003, in Society of Photo-Optical Instrumentation Engineers (SPIE) Conference Series, Vol. 4841, Society of Photo-Optical Instrumentation Engineers (SPIE) Conference Series, ed. M. Iye & A. F. M. Moorwood, 1670–1681
Li, I. H. & Yee, H. K. C. 2008, AJ, 135, 809
Loh, E. D. & Spillar, E. J. 1986, ApJ, 303, 154
McCracken, H. J., Radovich, M., Bertin, E., et al. 2003, A&A, 410, 17
Melinder, J., Mattila, S., Östlin, G., Mencía Trinchant, L., & Fransson, C. 2008, A&A, 490, 419
Metcalfe, N., Shanks, T., Campos, A., McCracken, H. J., & Fong, R. 2001, MNRAS, 323, 795
Metcalfe, N., Shanks, T., Fong, R., & Roche, N. 1995, MNRAS, 273, 257
Nonino, M., Dickinson, M., Rosati, P., et al. 2009, ApJS, 183, 244
Nuijten, M. J. H. M., Simard, L., Gwyn, S., & Röttgering, H. J. A. 2005, ApJ, 626, L77
Oesch, P. A., Bouwens, R. J., Carollo, C. M., et al. 2010, ApJ, 725, L150
Ouchi, M., Shimasaku, K., Okamura, S., et al. 2004, ApJ, 611, 660
Partridge, R. B. & Peebles, P. J. E. 1967, ApJ, 147, 868
Pickles, A. J. 1998, PASP, 110, 863
Pović, M., Sánchez-Portal, M., Pérez García, A. M., et al. 2009, ApJ, 706, 810
Radovich, M., Arnaboldi, M., Ripepi, V., et al. 2004, A&A, 417, 51
Rafelski, M., Wolfe, A. M., Cooke, J., et al. 2009, ApJ, 703, 2033
Rigopoulou, D., Vacca, W. D., Berta, S., Franceschini, A., & Aussel, H. 2005, A&A, 440, 61
Robin, A. C., Reylé, C., Derrière, S., & Picaud, S. 2003, A&A, 409, 523
Rovilos, E., Burwitz, V., Szokoly, G., et al. 2009, A&A, 507, 195
Sawicki, M. & Mallén-Ornelas, G. 2003, AJ, 126, 1208
Smail, I., Hogg, D. W., Yan, L., & Cohen, J. G. 1995, ApJ, 449, L105+
Steidel, C. C., Adelberger, K. L., Giavalisco, M., Dickinson, M., & Pettini, M. 1999, ApJ, 519, 1
Steidel, C. C., Giavalisco, M., Pettini, M., Dickinson, M., & Adelberger, K. L. 1996, ApJ, 462, L17+
Steidel, C. C. & Hamilton, D. 1993, AJ, 105, 2017
Stetson, P. B. 2000, PASP, 112, 925
Stoughton, C., Lupton, R. H., Bernardi, M., et al. 2002, AJ, 123, 485
Taniguchi, Y., Scoville, N., Murayama, T., et al. 2007, ApJS, 172, 9
Tinsley, B. M. 1972, ApJ, 173, L93+
van Breukelen, C., Clewley, L., Bonfield, D. G., et al. 2006, MNRAS, 373, L26
van der Burg, R. F. J., Hildebrandt, H., & Erben, T. 2010, A&A, 523, A74+
Vanzella, E., Cristiani, S., Arnouts, S., et al. 2002, A&A, 396, 847
Volonteri, M., Saracco, P., Chincarini, G., & Bolzonella, M. 2000, A&A, 362,

487
Wadadekar, Y. 2005, PASP, 117, 79
Wilson, G. 2003, ApJ, 585, 191
Yasuda, N., Fukugita, M., Narayanan, V. K., et al. 2001, AJ, 122, 1104
Yoshida, M., Shimasaku, K., Kashikawa, N., et al. 2006, ApJ, 653, 988
Yoshida, M., Shimasaku, K., Ouchi, M., et al. 2008, ApJ, 679, 269
Zhang, Y., Li, L., & Zhao, Y. 2009, MNRAS, 392, 233

## 9. Appendix A: SExtractor parameters

We present here the input (Table 10) and output (Table 11) SExtractor parameters. The parameters in bold are values that are intrinsic to each image, with aperture radius being $2 \times FWHM$ and detection area $FWHM^2 \times \frac{\pi}{4}$.

**Table 10.** SExtractor parameters used during the detection runs. Normal lettering correspond to parameters that are constant for all images, bold lettering represents those values that are intrinsic to each image.

| Parameter | Setting | Comment |
|---|---|---|
| PARAMETERS_NAME | default.param | Fields to be included in output catalog |
| FILTER_NAME | **gauss_FWHM_5x5.conv** | Filter for detection image |
| STARNNW_NAME | default.nnw | Neural-Network_Weight Table filename |
| CATALOG_NAME | STDOUT | Output to pipe instead of file |
| CATALOG_TYPE | ASCII | Output type |
| DETECT_TYPE | CCD | Detector type |
| DETECT_MINAREA | **int(FWHM$^2$*$\pi$/4)** | Minimum number of pixels above threshold |
| DETECT_THRESH | **$\leq$5% spurious detections** | Detection Threshold in $\sigma$ |
| ANALYSIS_THRESH | **$\leq$5% spurious detections** | Limit for isophotal analysis $\sigma$ |
| FILTER | Y | Use filtering |
| DEBLEND_NTHRESH | 64 | Number of deblending sub-thresholds |
| DEBLEND_MINCONT | 0.0 | Minimum contrast parameter for deblending |
| CLEAN | Y | Clean spurious detections |
| CLEAN_PARAM | 1 | Cleaning efficiency |
| MASK_TYPE | CORRECT | Correct flux for blended objects |
| PHOT_APERTURES | **2*FWHM** | MAG_APER aperture diameter(s) in pixels |
| PHOT_AUTOPARAMS | 2.5, 3.5 | MAG_AUTO parameters: <Kron_fact>,<min_radius> |
| PHOT_FLUXFRAC | 0.2,0.5,0.8,0.9 | Define n-light radii |
| PHOT_AUTOAPERS | 20.0, 20.0 | MAG_AUTO minimum apertures: estimation, photometry |
| SATUR_LEVEL | 50000 | Level of saturation |
| MAG_ZEROPOINT | **ZP** | Magnitude zero-point |
| GAIN | **n°ims*gain*exp.time** | Gain is 1 for absolute RMS map |
| PIXEL_SCALE | 0.205 | Size of pixel in arcseconds |
| SEEING_FWHM | **FWHM** | Stellar FWHM in arcseconds |
| BACK_SIZE | 64 | Background mesh in pixels |
| BACK_FILTERSIZE | 3 | Background filter |
| BACKPHOTO_TYPE | LOCAL | Photometry background subtraction type |
| WEIGHT_IMAGE | **weight-map** | Gain does not vary with changes in RMS noise |
| WEIGHT_TYPE | MAP_WEIGHT | Set Weight image type |
| MEMORY_PIXSTACK | 300000 | Number of pixels in stack |
| MEMORY_BUFSIZE | 1024 | Number of lines in buffer |
| MEMORY_OBJSTACK | 3000 | Size of the buffer containing objects |
| VERBOSE_TYPE | NORMAL | |

**Table 11.** Output data from SExtractor.

| Parameter | Comment |
|---|---|
| ID | identification number |
| MAG_APER | fixed aperture magnitude vector |
| MAGERR_APER | rms error vector for fixed aperture magnitude |
| MAG_AUTO | Kron-like elliptical aperture magnitude |
| MAGERR_AUTO | rms error for auto magnitude |
| ISOAREA_IMAGE | isophotal area above analysis threshold |
| X_IMAGE | x position in the image measured in pixels // object position along x |
| Y_IMAGE | y position in the image measured in pixels // object position along y |
| X_WORLD | right ascension // barycenter position along world x axis |
| Y_WORLD | declination // barycenter position along world y axis |
| THETA_IMAGE | positions angle (CCW/x) |
| ELLIPTICITY | 1 - B_IMAGE / A_IMAGE |
| FWHM_IMAGE | FWHM assuming a gaussian core |
| FLAGS | extraction flags |
| class-star | S/G classifier output |
| VECTOR_ASSOC | associated parameter vector |
| NUMBER_ASSOC | number of associated ID |